Zanganeh H, Srinil N. Three-dimensional VIV prediction model for a long flexible cylinder with axial dynamics and mean drag magnifications. *Journal of Fluids and Structures* 2016, 66, 127-146.

Three-Dimensional VIV Prediction Model for a Long Flexible Cylinder with Axial Dynamics and Mean Drag Magnifications

Hossein Zanganeh [a], Narakorn Srinil [b*]

[a] Department of Civil Engineering, University of Nottingham, United Kingdom

[b] School of Marine Science and Technology, Newcastle University, United Kingdom

Abstract

This study presents a three-dimensional phenomenological model for the analysis and prediction of vortex-induced vibration (VIV) of a long flexible circular cylinder in uniform flows, by taking into consideration the two salient effects of cylinder axial dynamics and mean drag magnifications. A semi-empirical theoretical model consists of structural nonlinear equations of coupled cross-flow, in-line and axial motions excited by vortex-induced hydrodynamic lift and drag forces. These forces are governed by two distributed and coupled wake oscillators describing the variations of lift and drag coefficients. This reduced-order model contains cubic and quadratic nonlinearities associated with geometric displacement couplings and fluid-structure interactions. A numerical finite difference approach combined with a frequency domain and modal analysis is used for analysing the highly nonlinear three-dimensional VIV responses. Several key features of flexible cylinder VIV are captured in the case of varying flow velocities. In particular, the dynamic responses exhibit a transition from standing to travelling wave characteristics, spatial dual 2:1 resonances with multi modal contributions, variable figure-of-eight trajectories, higher harmonic components, mean in-line/axial displacements and mean stresses as a result of VIV-amplified mean drag forces. Model validations are also performed through comparisons with published experimental results. Parametric studies highlight the individual and combined effects of geometric and hydrodynamic nonlinearities together with the axial dynamics which contribute to the space-time varying responses, frequencies, dominant modes and modal contributions, transverse bending and longitudinal stresses. Both quantitative and qualitative discrepancies are noticeable when the prediction model disregards these effects.

Keywords: VIV, flexible cylinder, 3-D response, axial dynamics, mean drag magnification, wake oscillator

* Corresponding author: narakorn.srinil@newcastle.ac.uk; Tel. +44 191 208 6499; Fax +44 191 208 5491

1. Introduction

Vortex-induced vibration (VIV) of a long flexible circular cylinder subject to a steady uniform flow generates several captivating fluid-structure interaction phenomena. Owing to the slenderness and inherent proneness to surrounding vortex-induced excitations, multi modes and frequencies of the flexible cylindrical structure can be three-dimensionally and simultaneously excited. These nonlinear oscillations with finite amplitudes take place in a wide range of practical flow velocities and can lead to critical bending and longitudinal stresses, increased fatigue damage and integrity loss of structural systems. To reach a fundamental understanding of flexible cylinder VIV and parametrically analyse the space-time varying dynamic behaviours, a computationally-robust three-dimensional (3-D) model accounting for combined structural geometric and hydrodynamic nonlinearities is needed.

From a structural geometry perspective, published works related to the cylinder VIV modelling, simulation and experiment can be categorised into two major groups which distinguish themselves between flexibly-mounted rigid (Bearman, 2011; Sarpkaya, 2004; Williamson and Govardhan, 2004) and flexible long (Brika and Laneville, 1993; Huera-Huarte and Bearman, 2009; Srinil, 2010; Vandiver, 1993; Wu et al., 2012) cylinders having two (cross-flow/in-line VIV) and multi degrees (multi modal cross-flow/in-line VIV) of freedom, respectively. For rigid cylinders, the use of a typical model of mass-spring-damper linear oscillator is justified, depending on the mass and damping ratios (Jauvtis and Williamson, 2004). However, the effects of geometric nonlinearities on response amplitudes and hydrodynamic properties can be meaningful (Srinil and Zanganeh, 2012; Srinil et al., 2013; Zanganeh and Srinil, 2014). For flexible long cylinders with initial straight configurations such as vertical top-tensioned risers (Srinil, 2011) and horizontal pipelines, a simplified linearized tensioned beam equation with transverse displacement in the cross-flow and/or in-line direction is mostly used in the literature (Violette et al., 2007). Nevertheless, this model neglects the axial oscillation which can be excited through its geometric coupling with cross-flow/in-line displacements (Srinil, 2010). The effect of axial motion can be salient for a cylinder with a high aspect (length-to-diameter) ratio, depending also on the structural extensibility and excited vibration modes (Srinil and Rega, 2008). Moreover, as the cylinder is greatly drifted by the VIV-amplified mean drag force, the axial mean displacement becomes meaningful. In this study, a 3-D flexible cylinder prediction model with a full coupling of cross-flow, in-line and axial nonlinear motions experiencing VIV due to combined lift and drag hydrodynamics is proposed and investigated, by also revealing the significant axial motion contributions.

With regard to the modelling of hydrodynamic forces, there have been a number of recent developments and modifications of so-called van der Pol wake oscillators for use in the prediction of flexible cylinder VIV. These have been driven mainly by the offshore oil and gas industry which requires an effective tool for the analysis and design of subsea risers, cables and pipelines in deep waters subjected to current-induced VIV. Previous studies which considered phenomenological wake oscillators focused on cross-flow-only VIV (Srinil, 2010; Violette et al., 2007), combined cross-flow/in-line VIV (Kim and Perkins, 2002; Srinil et al., 2009), and combined cross-flow/axial VIV (Xu et al., 2008). Some models have considered fixed (Facchinetti et al., 2004) or variable (Srinil, 2010; Srinil and Zanganeh, 2012) empirical coefficients, the latter depending on system physical parameters such as Reynolds number (Re) and mass ratio. These studies have revealed several capabilities of the wake oscillators in capturing key VIV features in qualitative and/or quantitative agreement with experimental observations and direct numerical simulations (Gabbai and Benaroya, 2005).

The key aspects of flexible cylinder VIV include the standing, hybrid standing-travelling and travelling wave characteristics, multi-mode sharing, switching and interactions, dual resonances and figure-of-eight orbital motions, higher harmonics contributing to fatigue damage, mean drag amplifications, and the key role of bending versus axial stiffness (Wu et al., 2012). Nonetheless, insights into the fully-coupled cross-flow, in-line and axial VIV are still lacking in the literature due to the use of a simplified linearized tensioned beam model. Therefore, the present study is aimed at overcoming such model limitation by further highlighting the important effects of axial displacements in conjunction with geometric nonlinearities and mean drag magnifications.

Experimental results and observations can also be used for calibration and validation of numerical predictions. Recently, a number of laboratory tests for flexible cylinder VIV have been carried out which witnessed some VIV behaviours found in rigid cylinder VIV (Govardhan and Williamson, 2006; Jauvtis and Williamson, 2004) and new aspects particularly for long slender cylinders (Chaplin et al., 2005; Lie and Kaasen, 2006; Vandiver et al., 2009). Song et al. (2011) performed a VIV test of a horizontal long flexible cylinder with aspect ratio of 1750 by towing it in a wave basin. They reported the asymmetry feature and higher harmonics in the cylinder spatial responses in uniform flows which are due to the multi-modal VIV. In this study, experimental model and parameters of Song et al. (2011) are used in the numerical investigations in order to validate the proposed 3-D prediction model and capture some flexible cylinder behaviours found experimentally.

The paper is structured as follows. In Section 2, the system nonlinear equations of 3-D motions of a long flexible cylinder undergoing VIV are presented along with the modelling of hydrodynamic lift and drag forces. In Section 3, numerical results in the case of varying flow velocities are discussed to highlight several capabilities of the model in capturing the flexible cylinder VIV behaviours and the effects of system parameters including the axial dynamics and VIV-amplified mean displacements. A model validation with numerical and experimental comparisons is addressed in Section 4. The paper ends with the conclusions in Section 5.

2. Three-Dimensional VIV Prediction Model

Figure 1(a) displays a schematic 3-D model of a long flexible circular cylinder subjected to a steady uniform flow of velocity V aligned with the in-line X direction. The fully-submerged cylinder is assumed to be perfectly straight at its vertical static equilibrium due to the effective weight. Pinned-pinned boundary conditions, which are typical for marine risers with flex joints as well as flexible cylinders in most experimental tests, are considered. However, other (e.g. clamped or moving) end conditions can also be imposed. For a long cylinder with a high aspect ratio, the effect of end boundaries could play an important role in the free-vibration characteristics, especially at higher-order modes, also depending on the structural stiffness properties. The cylinder is further assumed to behave in a linear elastic range of materials with a constant Young's modulus (E) and have spatially uniform properties including mass (m) and still-water added mass ($m_a=\rho\pi D^2/4$ with ρ being the fluid density) per length (L), damping coefficient (c), diameter (D), bending stiffness (EI), axial stiffness (EA_r), moment of inertia (I) and cross-sectional area (A_r).

Due to the *mean* drag force component in the in-line direction, the cylinder will statically displace and attend a planar (XY) curved configuration. Since the mean drag force can be further amplified due to the nonlinear coupling with VIV response (Blevins, 1990), the cylinder mean displacements will be further magnified. Subsequently, due to the combined effect of *hydrodynamic* lift and drag force components, the cylinder will oscillate three-dimensionally about this planar configuration in cross-flow (CF) Z, in-line (IL) X and axial (AX) Y directions.

2.1 Geometrically-nonlinear equations of flexible cylinder motions

By following Srinil et al. (2007; 2009), the nonlinear partial-differential equations of 3-D coupled CF, IL and AX motions of a flexible long cylinder can be expressed as

$$(m+m_a)\ddot{u} + c\dot{u} + EIu^{(IV)} - (Tu')' = EA_r(v''u' + v'u'') + \frac{1}{2}EA_r\left(3u''u'^2 + u''v'^2 + 2v''v'u' + u''w'^2 + 2w''w'u'\right) + F_x \quad (1)$$

$$(m+m_a)\ddot{v} + c\dot{v} + EIv^{(IV)} - (Tv')' = EA_r v'' + 2EA_r v''v' + EA_r(u''u' + v''v' + w''w') + \frac{1}{2}EA_r\left(v''u'^2 + 2u''u'v' + 3v''v'^2 + v''w'^2 + 2w''w'v'\right) + F_y \quad (2)$$

$$(m+m_a)\ddot{w} + c\dot{w} + EIw^{(IV)} - (Tw')' = EA_r(v''w' + v'w'') + \frac{1}{2}EA_r\left(w''u'^2 + 2u''u'w' + w''v'^2 + 2v''v'w' + 3w''w'^2\right) + F_z \quad (3)$$

in which u, v and w denote IL, AX and CF displacements, and F_x, F_y and F_z are the associated hydrodynamic forces, respectively. The overdot (prime) denotes derivative with respect to time t (space Y). The static effective tension T can be spatially varied by accounting for the buoyancy effect such that $T = T_t - g(m-\rho\pi D^2/4)Y$ where T_t is the top pre-tension and g is the gravity (Srinil, 2011). For a neutrally-buoyant vertical or horizontal cylinder, T is a constant (i.e. $T=T_t$) as considered in the experimental model of Song et al. (2011).

By accounting for large mean displacements and 3-D oscillations excited by the combined lift (F_L) and drag (F_D) forces, overall structural geometric nonlinearities and axial displacement couplings are accounted for through quadratic and cubic coupling terms in Eqs. (1)-(3). Hence, the proposed flexible cylinder model is more advanced and practical than a linear tensioned beam model (i.e. Eqs. (1) and (3) without nonlinear terms) typically considered in a great majority of research literature dealing with CF and IL VIV of flexible cylinders without AX motion effect.

2.2 Hydrodynamic forces with nonlinear coupling terms

Vortices generate oscillatory drag and lift forces with shedding frequencies of $2\Omega_f$ and Ω_f, respectively (Blevins, 1990). For a stationary cylinder whose projection is depicted in Fig. 1b, the drag and lift forces coincide with IL and CF directions, entailing $F_x = F_D$ and $F_z = F_L$. However, this might not be the case for an oscillating cylinder whose directions of apparent drag and lift forces can be arbitrary. Following a galloping theory (Blevins, 1990; Paidoussis et al., 2011), the total drag and lift forces may be assumed to act upon the cylinder section with a clockwise horizontal angle θ in the XZ plane and vertical angle γ in the XY plane, taking into account the relative velocities of the flow and the cylinder IL motion (V-$\dot{u}$), as shown in Fig. 1c. Accordingly, the projected three-dimensional fluid forces can be expressed as

$$F_x = F_L \cos\gamma \sin\theta + F_D \cos\gamma \cos\theta, \tag{4}$$

$$F_y = F_L \sin\gamma + F_D \sin\gamma, \tag{5}$$

$$F_z = F_L \cos\gamma \cos\theta - F_D \cos\gamma \sin\theta, \tag{6}$$

in which

$$F_D = \frac{1}{2}\rho D V_{rel}^2 (\bar{C}_d + C_D), \tag{7}$$

$$F_L = \frac{1}{2}\rho D V_{rel}^2 C_L, \tag{8}$$

where $\bar{C}_d$, C_D and C_L are the mean drag, oscillating drag and oscillating lift coefficients, respectively. The trigonometric functions in Eqs. (4)-(6) can be proved that $\cos\gamma\sin\theta = \dot{w}/V_{rel}$, $\cos\gamma\cos\theta = (V - \dot{u})/V_{rel}$ and $\sin\gamma = \dot{v}/V_{rel}$, in which the total velocity relative to the oscillating cylinder reads

$$V_{rel} = V\sqrt{\left(1 - \frac{\dot{u}}{V}\right)^2 + \left(\frac{\dot{v}}{V}\right)^2 + \left(\frac{\dot{w}}{V}\right)^2}. \tag{9}$$

For a small $\dot{v}$ or large V_{rel}, γ becomes very small such that $\sin\gamma \approx 0$, yielding $F_y \approx 0$ and $\cos\gamma \approx 1$, see Fig. 1d. Accordingly, Eqs. (4) and (6) become

$$F_x = F_L sin\theta + F_D cos\theta, \tag{10}$$

$$F_z = F_L cos\theta - F_D sin\theta. \tag{11}$$

Above Eqs. (10) and (11) have been successfully utilised in VIV studies on elastically-mounted rigid cylinders (Dhanwani et al., 2013; Zanganeh and Srinil, 2014), and they can be applied to a flexible cylinder VIV analysis if the influence of γ is proved to be negligible (see Section 3.1 for the analysis results and discussion).

Following the pioneering idea of Bishop and Hassan (1964) who noted that the vortex shedding in the wake behaves like an oscillator, the fluctuation of drag and lift forces may be modelled using the van der Pol oscillators with cylinder acceleration coupling terms (Facchinetti et al., 2004). By introducing the wake variables $p = 2C_D/C_{d0}$ (Srinil and Zanganeh, 2012) and $q = 2C_L/C_{l0}$ (Facchinetti et al., 2004) where C_{d0} and C_{l0} are the associated drag and lift coefficients of a stationary cylinder, the variations of p and q may be described through

$$\ddot{p} + 2\varepsilon_u \Omega_f (p^2 - 1)\dot{p} + 4\Omega_f^2 p = \frac{\Lambda_u}{D}\ddot{u} \tag{12}$$

$$\ddot{q} + \varepsilon_w \Omega_f (q^2 - 1)\dot{q} + \Omega_f^2 q = \frac{\Lambda_w}{D}\ddot{w} \tag{13}$$

where $\Omega_f = 2\pi \mathrm{St} V/D$ and St is the Strouhal number (assumed as 0.18 following Song et al. (2011)). ε_u, ε_w, Λ_u and Λ_w are empirical coefficients which can be tuned via model calibration with experimental results. By substituting Eqs. (7)-(9) and (12)-(13) into Eqs. (4)-(6), overall hydrodynamic force components read

$$F_x = \frac{1}{4}\rho D V_{rel} C_{l0} q\dot{w} + \frac{1}{4}\rho D V_{rel} C_{d0} p(V - \dot{u}) + \frac{1}{2}\rho D V_{rel} \bar{C}_d (V - \dot{u}), \tag{14}$$

$$F_y = \frac{1}{4}\rho D V_{rel} C_{l0} q\dot{v} + \frac{1}{4}\rho D V_{rel} C_{d0} p\dot{v} + \frac{1}{2}\rho D V_{rel} \bar{C}_d \dot{v}, \tag{15}$$

$$F_z = \frac{1}{4}\rho D V_{rel} C_{l0} q(V - \dot{u}) - \frac{1}{4}\rho D V_{rel} C_{d0} p\dot{w} - \frac{1}{2}\rho D V_{rel} \bar{C}_d \dot{w}. \tag{16}$$

Inspecting above expressions reveals several important aspects summarized as follows.

- Eq. (14) contains a static mean drag force which is, to first order, proportional to the flow velocity squared. Higher-order nonlinear effects are also accounted for through the square root term in Eq. (9).
- Eqs. (14)-(16) contain the time-varying hydrodynamics which are temporally and spatially coupled with cylinder CF, IL and AX oscillations via quadratic nonlinear terms $p\dot{u}$, $q\dot{w}$, $q\dot{u}$, $p\dot{w}$, $q\dot{v}$ and $p\dot{v}$. These quadratic nonlinearities have been found to be responsible for dual 2:1 resonances and associated figure-of-eight appearances (Srinil and Zanganeh, 2012).
- The first term in Eq. (14) entails the additional cylinder drift which depends on CF amplitudes. This term leads to the mean displacement amplified by VIV (Zanganeh and Srinil, 2014).
- The terms with $\bar{C}_d \dot{u}$, $\bar{C}_d \dot{v}$ and $\bar{C}_d \dot{w}$ give rise to the fluid-added damping, typically called the stall parameter, which provides a self-limiting cylinder response at zero structural damping (Skop and Balasubramanian, 1997).
- Choices for C_{d0}, C_{l0} and $\bar{C}_d$ corresponding to a stationary cylinder are variable in the literature, depending on e.g. Re and surface roughness. Randomness of these parameters could be treated (Low and Srinil, 2016). However, herein a single set of C_{d0}=0.2 (Currie

and Turnbull, 1987), C_{l0}=0.3 and $\bar{C}_d \approx 1.2$ (Blevins, 1990) is used. These values are suitable for a cylinder with smooth surface and subject to a sub-critical flow with the maximum Re of about 2x10^5 (Blevins, 1990); thus, they are valid for the Re range of 3000-15000 considered in the parametric studies in Sections 3 and 4.

With regard to the tuning parameters in Eqs. (12) and (13), we assume ε_u=0.3, Λ_u=12 and Λ_w=12 based on recent calibration in Srinil and Zanganeh (2012) for rigid cylinders. To make one of the empirical coefficients depend on system parameters, Eq. (35) in Facchinetti et al. (2004) and Eq. (6.2) in Govardhan and Williamson (2006) are combined which lead to a unique analytical expression for ε_w as

$$\varepsilon_w = \frac{\Lambda_w}{4\frac{\mathrm{S_G}+1.3}{C_{l0}}\left(2\frac{\mathrm{S_G}+1.3}{C_{l0}}(1-1.12\alpha+0.3\alpha^2)\log 0.41\mathrm{Re}^{0.36}\right)^2-1} \tag{17}$$

in which $\mathrm{S_G}$ and α are the combined mass-damping parameters defined as $S_G = 2\pi^3 St^2 m^* \xi$ and $\alpha = (m^* + C_A)\xi$, $m^*=m/(\rho\pi D^2/4)$ the mass ratio, ξ the damping ratio and C_A the still-water added mass coefficient taken as unity for a circular cylinder (Blevins, 1990). For a given Λ_w, α, $\mathrm{S_G}$ and C_{l0}, ε_w decreases with increasing Re. This would enhance VIV response due to the lower damping value in the wake oscillator through Eq. (13).

Note that the assumed empirical coefficients (ε_u, Λ_u, ε_w, Λ_w) are based on calibration with experimental results of elastically-mounted rigid cylinders (Facchinetti et al., 2004; Srinil and Zanganeh, 2012) as well as those (Song et al., 2011) of a specific flexible cylinder considered herein. The original fixed value of ε_w=0.3 (Facchinetti et al., 2004) or the variable ε_w value as a function of m^* (Srinil et al., 2013) was found to be insufficient to capture the spatially-maximum values of the root-mean-squared responses of such flexible cylinder. Therefore, Eq.(17) is recommended to yield reasonably comparable numerical-experimental results (see Section 4) and to follow recent experimental observations of actual risers with VIV dependence on the Re and mass-damping parameters (Swithenbank et al., 2008). At present, a universal wake oscillator model and associated empirical coefficients do not coexist; however, a better calibration procedure with several flexible cylinder VIV experiments, if available, should be carried out by taking into account the effects of e.g. aspect ratio, modal shape, modal damping and multi modal interaction, not found in rigid cylinders.

Highly nonlinear partial-differential Eqs. (1)-(3) in conjunction with Eqs. (12)-(13) are numerically solved for 3-D responses of the flexible cylinder undergoing VIV by using a finite difference approach in both space and time domain (see Appendix A). Initial conditions are

specified at the static equilibrium for the cylinder ($u = v = w = \dot{u} = \dot{v} = \dot{w} = 0$), with p=2 ($\dot{p} = 0$) and q=2 ($\dot{q} = 0$) for wake variables. Calibration and convergence tests of numerical simulations with the considered experimental cylinder of Song et al. (2011) have been performed and the following results are based on the time step of 0.0001 s and 57 spatially discretised elements. Insights into flexible cylinder VIV aspects captured by the presented model are presented in Section 3 whereas model validation with experimental results are shown in Section 4.

3. Numerical Results and Discussion

A long flexible cylinder model experimentally tested by Song et al. (2011) is considered. The horizontally-oriented and straight cylinder has a practical aspect ratio (L/D) of 1750 and low m^*=1. A range of ξ<0.01 was reported; herein, ξ=0.01 is assumed. Due to such a neutrally buoyant condition, there is no effect of initial pre-tension variation or submerged weight on the static configuration. The flow past the cylinder is spatially uniform with velocity of 0.18-0.60 m/s in the sub-critical Re range of 3000-10000. With cylinder bending (153.71 N.m^2) and axial (5.11×10^6 N) stiffness properties, CF and IL vibrations were reported at modes up to the 6th and 12th, respectively. No axial motions were discussed in Song et al. (2011); however, their effects are herein highlighted through numerical studies. In the following, prediction results with specified V=0.3, 0.4, 0.8 and 1 m/s are presented for the cylinder with pre-tension of 700 N. Higher V than 0.60 m/s are also considered so that the high-mode VIV aspect can be realized.

3.1 Three-dimensional cross-flow, in-line and axial VIV responses

The influence of the vertical angle γ(Fig. 1c) is first examined by comparing the obtained responses based on the 2-D (Eqs. 10-11) vs 3-D (Eqs. 4-6) projection of hydrodynamic forces. In Fig. 2, the cylinder responses associated with the 2-D (Fig. 2a-e) and 3-D (2f-j) fluid force models are displayed, considering the maximum V = 1 m/s. At the steady state, CF (Fig. 2a and f), IL (Fig. 2d and i) and AX (Fig. 2e and j) oscillation components, as well as total IL (Fig. 2b and g) and AX (Fig. 2c and h) displacements inclusive of mean and oscillatory values, are compared. Results in Fig. 2 reveal how overall responses are qualitatively and quantitatively very similar and comparable, regardless of the considered hydrodynamic model. Therefore, the γ angle effect can be negligible for such flexible cylinder subject to the considered V range up to 1 m/s. To reduce the computational effort, the 2-D transverse hydrodynamic model only accounting for the horizontal angle θ effect is considered in the following.

For a given V = 0.3 and 0.8 m/s, Fig. 3 illustrates the space-time varying CF (3a, 3d), IL (3b, 3e) and AX (3c, 3f) responses including initial transient and steady-state dynamics ($0<t<50$ s). Combined mean and oscillatory components are plotted in Fig. 3 whereas only the extracted oscillatory components within certain steady-state periods ($99<t<100$ s) are shown in Fig. 4 along with other cases of V = 0.4 and 1 m/s. It can be seen in Fig. 3 that transient periods required for yielding the steady-state responses increase with V and modes being excited. Depending on initial conditions, a prompt switching from the standing wave to the travelling wave is noticed in CF response at higher V (Fig. 3d). Large mean displacements are clearly visible in IL responses (see Fig. 3b vs. 4e and Fig. 3e vs. 4g) and they increase considerably with V. Smaller – but appreciable – mean AX displacements are also noticed (see Fig. 3c vs 4i and Fig. 3f vs 4k). From Fig. 3, spatial IL profiles are symmetric (Fig. 3b, 3e) whereas spatial AX profiles are anti-symmetric (Fig. 3c, 3f), with respect to the middle span. Because the cylinder is displaced due to the mean drag force, the coexisting symmetric IL and anti-symmetric AX mode shapes establish a planar vibration of the curved cylinder as known from the theory of cable dynamics (Srinil and Rega, 2007). By comparing Figs. (3a) vs (4a) and (3d) vs (4c), no mean components are observed in the CF direction. This is expected since the uniform flow pasts the straight cylinder (Chaplin et al., 2005).

In further view of Fig. 4, several aspects can be remarked with increasing V, which confirm experimental observations of flexible cylinder VIV (Tognarelli et al., 2004). In general, overall responses are governed by the standing wave characteristics at low V = 0.3 and 0.4 m/s (Fig. 4a, 4b, 4e, 4f, 4i and 4j) whereas the travelling wave responses appear at higher V = 0.8 and 1 m/s involving higher-order modes (Figs. 4c, 4d, 4g, 4h, 4k and 4l). IL and AX oscillation frequencies are nearly twice the CF oscillation frequencies, see, e.g., sections A-A vs B-B and C-C in Figs. 4(a) vs 4(e) and 4(i). Hence, the cylinder undergoes higher vibration modes in IL and AX directions due to greater vortex shedding frequencies of $2\Omega_f$. The space-time varying plots also suggest the single-mode CF oscillations whereas IL and AX responses signal some multi modal aspects. A modal analysis is performed in Section 3.2 to distinguish contributing modes.

In terms of spatially and temporally maximum responses, Fig. 4 demonstrates that all CF, IL and AX amplitudes increase as V increases. This is in agreement with field experimental results of Swithenbank et al. (2008) who suggested the increasing response amplitudes with Re. The importance of increasing AX motions should also be noted at higher V since this will affect the dynamic tension and in turn the longitudinal stress as further discussed in Section 3.4.

3.2 Oscillation frequencies and multi modal contributions

A frequency domain analysis of obtained time histories is now performed using a Fast Fourier Transform to identify 3-D oscillation frequencies (f_o) along cylinder span. The power spectral densities (PSD) associated with Fig. 4 are presented in Fig. 5. Results show the increasing frequencies with V in all responses and confirm how IL and AX dominant frequencies associated with planar modes are nearly twice CF ones in all considered V. These dominant fundamental harmonics justify dual 2:1 resonances which appear uniformly along the span. Higher oscillation frequencies are also captured with the third and fourth harmonics in the CF and IL/AX directions, respectively. In addition, at higher V = 0.8 and 1 m/s, the higher sixth harmonics also come into play in both IL (Fig. 5h) and AX (Fig. 5k and 5l) directions although they have relatively small amplitudes. These findings emphasize the importance of higher harmonics which could contribute to the fatigue damage as recently reported in several experimental studies (Mukundan et al., 2009), and show the additional feature of coexisting axial oscillations through the present 3-D model. A more sophisticated procedure for the frequency analysis can alternatively be considered (Franzini et al., 2014).

To identify which and how many modes participating in each VIV response, a standard linear modal analysis is now performed based on the approach proposed by Lie and Kaasen (2006) and subsequently considered by Song et al. (2011). For the flexible cylinder with pinned-pinned end conditions, the time-varying modal displacements with removed mean components at each node i ($\Upsilon_i(t)$, i=1,2,..I) in each CF (w), IL (u) and AX (v) direction may be approximately projected onto a series of sinusoidal functions $\varphi_j(Y)=\sin(j\pi Y/L)$ as

$$\Upsilon_i(t) = \sum_{j=1}^{J} W_j(t)\varphi_j(Y_i) \tag{18}$$

where j is the mode order (j=1,2,..J), J the number of modes and $W_j(t)$ the associated modal weight. Such sine series can be assumed for the AX oscillation as noted in Rao (2007). They have been used by Srinil et al. (2009) for the IL/AX eigenfunction analysis of a catenary riser and practically recommended by Tognarelli et al. (2004) for use in the modal analysis of vertical cylinders exhibiting both standing- and travelling-wave responses. Since the response is obtained at each spatial node i, one can write Eq.(18) in a matrix form as

$$\overline{\Upsilon} = \Theta\overline{W} \tag{19}$$

where the vectors $\overline{\Upsilon} = \left[\Upsilon_1(t), \Upsilon_2(t), ...\Upsilon_I(t)\right]^T$ and $\overline{W} = \left[W_1(t), W_2(t), ...W_J(t)\right]^T$. The IxJ matrix $\Theta = \left[\Theta_1, \Theta_1, ...\Theta_J\right]$ with $\Theta_j = \left[\varphi_j(Y_1), \varphi_j(Y_2), ...\varphi_j(Y_I)\right]^T$. By considering $J = I$ as in

this study, the modal weights at each time step can be extracted from $\overline{W} = \Theta^{-1}\overline{\Upsilon}$. By performing the FFT analysis of $\overline{W}$ time series, each modal power can be obtained and the dominant modes can be decided based on the power ranking. In the case of $J < I$, the least-squares approach should be implemented (Lie and Kaasen, 2006).

Based on the space-time varying responses in Fig. 4 and oscillation frequencies in Fig. 5, the associated modal contents are plotted in Fig. 6 with the sine-mode number (n =1-20) labelled along the outer circumference and the associated modal powers along the radial axes. Note that odd numbers (n = 1, 3, 5,…) represent symmetric modal shapes whereas even numbers (n = 2, 4, 6,…) represent anti-symmetric modal shapes. Each modal power is normalized with the largest one and represented by a different colour in each direction so that the maximum (minimum) value is unity locating at the outer circle (centre).

At low V = 0.3 and 0.4 m/s where standing waves dominate the responses, it can be seen that CF motions are single-mode VIV whereas IL and AX motions undergo multi modal VIV. The latter supports the study of Srinil (2010) who proposed a multi-mode VIV analysis of a curved cylinder involving planar responses. When CF spatial profiles are symmetric with dominant n = 3 (Fig. 6a vs 6a) at V = 0.3 m/s, IL profiles are symmetric with dominant (n = 5) and contributing (n = 1, 3 and 7) modes (Fig. 6a vs 4e) whereas coexisting AX profiles are anti-symmetric with dominant (n = 4) and contributing (n = 2, 6 and 8) modes (Fig. 6a vs 4i). With increasing V = 0.4 m/s (Fig. 6b), the CF sine mode becomes anti-symmetric as shown in Fig. 4b with n = 4 whereas IL (AX) sine modes maintain their pre-dominant symmetric (anti-symmetric) characters as shown in Fig. 4f (4j) with dominant n = 7 (n = 6) mode. These findings are in consistent with the cable dynamics theory regarding the nonlinear orthogonal properties of modes for which 2:1 resonances involve high-frequency symmetric IL planar modes and low-frequency symmetric or anti-symmetric CF out-of-plane modes (Srinil et al., 2004).

At high V=0.8 and 1 m/s where travelling waves dominate (Fig. 6c and 6d), multi-mode VIV now take place in all CF, IL and AX responses involving hybrid symmetric and anti-symmetric modal contributions. Nevertheless, the linear modal approach based on the standing-wave modes might not be suitable to identify varying amplitudes and phase differences. In the latter case, a nonlinear modal analysis with complex-valued modes (Vandiver et al., 2009) should be alternatively considered.

3.3 Motion trajectories and mean drag magnification effect

Figure 7 displays orbital motions at different locations along cylinder span by

characterising IL-CF (*u*-*w*), IL-AX (*u*-*v*) and AX-CF (*v*-*w*) trajectories at two different specified *V*. Regardless of actual amplitudes, the plots in Fig. 7 are scaled up for visibility purpose. Due to the presence of dual 2:1 resonances as shown in Fig. 5, most of the IL-CF trajectories reveal the repeatable figure-of-eight shapes with variable phase differences and some modulations. These confirm what have been experimentally observed in the literature for flexible cylinder VIV (Vandiver et al., 2009). The effect of increasing *V* and Re is highlighted by the travelling wave characteristics and greater multi modal contributions at *V* = 1 m/s which contribute to the non-similar patterns of the trajectories at opposite locations with respect to the middle span (*Y/D* = 875) in comparison with the lower *V* = 0.3 m/s case. For IL-AX trajectories, both 1:1 and 1:2 resonant motions do dominate at different locations with the latter being due to the higher harmonic effect. These suggest the spatial variations of bending and longitudinal stresses and the associated fatigue, depending on the oscillation frequencies and their harmonics.

Figure 8 illustrates the total mean IL (Fig. 8a) as well as AX (Fig. 8b) deflections along the cylinder span at different *V* from 0.1 to 1 m/s. It can be seen that the mean deflections (normalized by *D*) increases with *V* due to the drag magnifications caused by VIV. The highest mean values up to about 30*D* in the IL direction and 0.5*D* in the AX direction can be realized at highest *V*, the former being similar to what has been reported in Huera-Huarte (2006). Figure 8(b) also illustrates that while the cylinder undergoes an anti-symmetric axial deflection profile at low *V*, the latter becomes asymmetrical at higher *V*. This is due to the dependence and coupling of mean drag on CF oscillations whose amplitudes travel through waves along the span producing asymmetric CF oscillation at high *V*.

3.4 Evaluation of transverse bending and longitudinal stresses

Numerical responses can now be used for the evaluation of transverse bending and longitudinal stresses. To achieve this, approximations of maximum compressive (-) and tensile (+) bending stresses in CF and IL directions, σ_w and σ_u, respectively, are evaluated through

$$\sigma_w(Y,t) \approx \pm\frac{D}{2}Ew''(Y,t) \tag{20}$$

$$\sigma_u(Y,t) \approx \pm\frac{D}{2}Eu''(Y,t) \tag{21}$$

whereas the longitudinal stress σ – accounting for overall displacement components – can be approximated by (Srinil et al., 2007)

$$\sigma(Y,t) \approx E\left(v' + \frac{1}{2}(u'^2 + v'^2 + w'^2)\right) \tag{22}$$

It is important to emphasize that overall CF, IL and AX responses, inclusive of mean and oscillatory components, contribute to the longitudinal stresses. Figure 9 displays total CF bending (Fig. 9a, 9d), IL bending (Fig. 9b, 9e) and longitudinal (Fig. 9c, 9f) stresses at low and high V, in association with the displacement plots in Figs. 3 and 4.

At low V = 0.3 m/s where responses are standing waves, maximum (minimum) CF bending stresses shown in Fig. 9a, see section A-A, occur at locations of maximum displacements (nodes) shown in Fig. 4a corresponding to a symmetric mode. The time variation of σ_w is illustrated by section B-B in Fig. 9a which shows a transition of maximum tensile and compressive stresses for a specific location. At the nodes, section C-C in Fig. 9a maintains the constantly zero σ_w vs time. The effect of higher frequencies on the bending stress is highlighted by section B-B vs D-D in Fig. 9a where for a certain range of oscillation the latter exhibits periodically a greater number of peaks. This is in accordance with section E-E which shows spatially 6 peaks against 3 peaks in section A-A. These signals the potentially greater fatigue damage locations although with lower stress values. For multi-mode IL VIV involving higher-order modes due to the doubled frequencies, the associated σ_u plots in Fig. 9b reveal a more complicated pattern of maximum and minimum stresses whose several specific locations can be identified following the dominant standing waves.

At higher V = 0.8 m/s, travelling waves dominate in CF and IL bending stress plots as shown in Figs. 9d and 9e, resulting in the remarkable spatial variation of locations involving maximum and minimum stresses. Throughout the cylinder span is potentially subject to the critical fatigue damage. Overall, both CF and IL (tensile and compressive) bending stresses increase considerably with V due to increasing curvatures, and their magnitudes are within the same orders. These highlight how one cannot neglect the IL stress contributions although IL amplitudes are smaller than CF amplitudes, and confirm what have been witnessed from full-scale tests of riser VIV (Tognarelli et al., 2004).

The associated longitudinal stresses σ are displayed in Fig. 9c (V=0.3 m/s) and 9f (V=0.8 m/s). The spatial patterns appear relatively uniform at lower V (Fig. 9c) but with a greater span-wise variation at higher V (Fig. 9f), depending on the combination of multi symmetric/anti-symmetric CF, IL and AX modes as well as the standing vs travelling wave characteristics. Overall, the total longitudinal stresses are of tensile type, considerably increasing with V due to the VIV-amplified mean IL and AX displacements (Fig.8).

Together with Fig.9, Table 1 provides a summary of maximum and minimum values of *total* bending and longitudinal stresses at four different V. Results highlight the significance of total longitudinal stresses. Total IL bending stresses become greater than total CF ones at higher V, with the former exhibiting unequal maximum and minimum stresses: this suggests the asymmetry effect caused by amplified mean displacements and multimode contributions. Critical total IL bending stresses are more compressive, signalling the potential dynamic buckling issue. By removing the time-averaged mean components as in Table 2, overall bending and longitudinal stresses highlight their increasing values with V, becoming more tensile and compressive. Such amplifications and combinations of stresses are critical from a structural fatigue design viewpoint since in practice longitudinal stresses have typically been overlooked through using a linearized beam model with only transverse vibrations.

3.5 Effects of axial dynamics, geometric and hydrodynamic nonlinearities

The importance of AX VIV through the modelling and prediction is now highlighted in Fig. 10 in terms of root-mean-squared (RMS) CF (Fig. 10a and c) and IL (Fig. 10b and d) amplitudes (spatially and temporally averaged), and amplified drag-induced mean displacements (Fig. 10e). With respect to Eqs. (1)-(3), three prediction models are simulated including (i) the present fully nonlinear model (blue circles), (ii) the geometrically linearized model but still accounting for the equation of axial motion (pink squares), and (iii) the full nonlinear model without axial motion (black diamonds). Two V cases (0.3 and 0.8 m/s) are considered and the quadratic nonlinearities governing the coupled hydrodynamic forces are accounted for in all simulation cases.

At low V=0.3 m/s, the effect of geometric nonlinearities plays the most significant role since model (ii) produces both quantitatively and qualitatively different results of both CF (Fig. 10a) and IL (Fig. 10b) amplitudes when compared with those predicted by other two models. In particular, the dominant CF (n=5) and IL (n=9) modes of the model (ii) are incorrectly higher than the dominant CF (n=3) and IL (n=5) modes of the models (i) and (iii). The effect of axial motion is seen to be relatively small for such low V since results of model (i) and (iii) are comparable with some small amplitude differences.

As V increases to 0.8 m/s, the effect of axial motion now becomes pronounced as does the effect of geometric nonlinearities since the model (iii) entails CF (Fig. 10c) and IL (Fig. 10d) responses quantitatively and qualitatively different from those predicted by model (i). The worst scenario takes place with model (ii). Therefore, both the effects of geometric nonlinearities and axial displacement coupling are important in the VIV prediction at higher V.

In view of the amplified mean displacements shown in Fig. 10e for V=0.3 m/s, one can realize when compared with the full nonlinear model that, even at low V, the model neglecting the axial motion underestimates the mean displacement values and therefore the mean tension and longitudinal stresses. On the contrary, the model excluding geometric nonlinearities can render considerably overestimated results which are typical for a linear model (Srinil, 2010).

Of theoretical and practical importance, the individual effects of neglecting the axial motions, the geometric and hydrodynamic nonlinearities are now highlighted through Fig. 11 in comparison with results in Fig.4 based on a complete nonlinear 3-D model. The space-time varying CF (Fig.11a, b and c vs Fig.4c) and IL (Fig.11d, e and f vs Fig.4g) responses are plotted with V=0.8 m/s. Considerations include: (i) the model with geometric and hydrodynamic nonlinearities but with omitted axial motions (Fig.11a and d); (ii) the model with geometric nonlinearities but with omitted hydrodynamic nonlinearities and axial motions; (iii) the fully linearized model with omitted axial motions. Results in Fig.11 highlight that:

(i) When neglecting the axial motions, both CF (Fig.11a) and IL (Fig.11d) responses increase (see also Fig.10c and d) and their travelling-wave features disappear.

(ii) When further neglecting the hydrodynamic nonlinearities (i.e. Fig.1b), CF responses considerably increase by achieving an unrealistic maximum amplitude per diameter of about 4. This is too overestimated. In addition, the space-time varying profiles of both CF (Fig.11b) and IL (Fig.11e) responses quantitatively and qualitatively change, in terms of features and modes being excited.

(iii) Finally, when considering a fully-linearized model without axial motion, i.e. the 2-D linear model often considered in the literature for flexible cylinder VIV, CF responses further increase while IL responses decrease. Both CF (Fig.11c) and IL (Fig.11f) responses appear to be purely single-modal and standing-wave types which are in contrast with those based on the full nonlinear model exhibiting multi-mode and travelling-wave responses.

In summary, above quantitative and qualitative differences with different levels of model approximation must be seriously taken into consideration in the prediction model as well as experimental post-processing analysis for flexible cylinder VIV. Inaccurate response amplitude predictions can lead to the erroneous estimation of maximum bending/longitudinal stresses and the associated fatigue. The most simplified model renders the standing waves even at high-order modes. This can further lead to a misunderstanding of critical locations where high stresses and fatigue take place.

4. Model Validation with Numerical and Experimental Comparisons

Previous prediction results have highlighted the importance of considering the axial dynamic coupling, the amplification of IL mean displacements, the geometric and hydrodynamic nonlinearities. In the following, numerical prediction results based on the fully nonlinear 3-D model are compared with experimental post-processed results of Song et al. (2011). Note that experimental discussion on the axial VIV was not reported, and this may in part a source of some differences in the comparisons in addition to the lack of actual ξ.

Figures 12a and 12b display numerical and experimental comparisons of obtained maximum CF (A_{wM}/D) and IL (A_{uM}/D) amplitudes vs V whereas Figs. 12c and 12d present the associated RMS results (A_{wRMS}/D, A_{uRMS}/D) vs V_r, respectively. Note that $V_r = V/f_oD$ with f_o being the dominant oscillation frequency (Fig.5). In Fig. 12a, dashed lines are also added to distinguish a trend of numerical CF results which behaves like a saw-tooth in comparison with relevant experimental results (with a group of coloured squares). The saw-tooth trend with a dropping and growing amplitude pattern takes place when the response switches from one branch of the dominant mode to another as V increases (Chaplin et al., 2005). With respect to the amplitude values, a satisfactory agreement is seen in the CF response with numerical maximum A_{wM}/D of about 1.7 and experimental maximum A_{wM}/D of about 1.6 (Fig. 12a). In contrast, a greater difference occurs in the IL response comparison with numerical maximum A_{uM}/D of about 0.4 and experimental maximum A_{wM}/D of about 0.7 (Fig. 12b). Nevertheless, overall comparisons are improved once the RMS values are statistically considered as shown in Figs. 12c and 12d for CF and IL responses, respectively. The RMS amplitudes are typically recognized in the literature dealing with experimental studies to rule out any uncertainties and nonlinearities that may have arisen during the tests. In addition, when plotting the amplitudes vs V_r in Fig.12c and 12d, overall numerical-experimental results compare well, with maximum responses taking place within the excitation V_r range of about 3-7 for each dominant mode.

Numerical-experimental comparisons of response dominant frequencies and modes are displayed in Figs. 13a and 13b, respectively. In Fig. 13a, a good agreement can be seen where both experimental and numerical results reveal how their oscillation frequencies linearly increase with V by following the Strouhal law in both CF and IL directions. In particular, IL frequencies are nearly twice CF frequencies which confirm the occurrence of 2:1 dual resonances involving combined CF and IL VIV. These dual resonances have been observed in VIV experiments of elastically-mounted rigid (Dahl et al., 2010) and long flexible cylinders (Wu et al., 2012). With respect to dominant modes shown in Fig. 13b, comparisons reveal how, within a moderate and high V range, the orders of experimental IL modes are higher than those

of numerical ones. Although CF mode orders produce a better agreement, we are unable to comment on such IL differences and how experimental results have been post-processed. Yet, we can only note, by referring to a sentence in Song et al. (2011) that "*the values at high velocity cases might be a little overestimated…This is because the estimates of the displacement are sensitive to the judgement of the lowest mode*". Apart from that, the combined effects of axial dynamics, geometric nonlinearities and actual modal ξ could play an influential role.

5. Conclusions

A 3-D fluid-structure interaction model for the analysis and prediction of coupled cross-flow, in-line and axial VIV of a long flexible circular cylinder in uniform flows is presented. This computationally-efficient phenomenological model with the application of distributed wake oscillators accounts for two salient effects of cylinder axial dynamics and mean drag magnifications through overall geometric and hydrodynamic nonlinearities. These cubic and quadratic nonlinearities are associated with the cylinder large displacements and coupling of oscillatory lift, oscillatory drag and mean drag forces. A space-time finite difference approach has been applied to perform direct numerical integrations of system highly nonlinear partial-differential equations of coupled hydrodynamic-cylinder motions. In the case of increasing flow velocities V, insights into several VIV nonlinear dynamic phenomena governing a long flexible cylinder with a low mass ratio are captured by the proposed theoretical model. The key aspects are summarized as follows.

- As a result of steady and amplified mean drag forces, the flexible straight cylinder becomes curved in a planar configuration about which VIV in-plane and out-of-plane modes can be distinguished. In-plane modes comprise axial and in-line components whereas out-of-plane modes are associated with cross-flow components.
- Standing (single- and multi-mode) and travelling (multi-mode) wave characteristics are observed through the space-time varying responses, with travelling waves taking place from a moderate V and involving high-mode and high-frequency VIV. A transition from standing to travelling waves at a certain V is also found, depending on the initial conditions and transient dynamics.
- Spatial dual 2:1 (in-line:cross-flow and axial:cross-flow) resonances reveal multi modal contributions and variable figure-of-eight trajectories with amplitude modulations due to higher harmonic components and multi-mode interactions. In agreement with the cable dynamics theory (Srinil et al., 2004), VIV 2:1 resonances of the flexible cylinder involve

high-frequency symmetric in-line (planar) modes and low-frequency symmetric or anti-symmetric cross-flow (out-of-plane) modes.

- Due to the VIV-amplified mean drag forces, mean in-line and axial displacements increase with V. These lead to a considerable magnification of total longitudinal stresses whose values can be higher than the associated transverse bending stresses. Moreover, the overall combination of oscillatory bending and longitudinal stresses increases with V. These are crucial from a structural strength and fatigue design viewpoint.
- The individual and combined effects of axial dynamics, geometric and hydrodynamic nonlinearities are significant. Depending on system parameters, V and the associated excited modes, the fully linearized model can lead to both quantitative and qualitative discrepancies giving rise to inaccurate estimations of 3-D response amplitudes, dynamic features, modal contributions, mean displacements and transverse/longitudinal stresses.

Partial model validations have been performed through comparisons with experimental results in the literature. Results show some agreements and differences which require further improvement of empirical coefficients and experimental studies for flexible cylinder 3-D VIV with a reliable post-processing approach accounting for the axial dynamics and system nonlinearities. Apart from capturing several VIV phenomena, the proposed model could be used as an efficient tool in the early-stage design of offshore cylindrical structures in currents. Non-uniform sheared flow cases can also be considered although with the lesser effect of axial dynamics (Zanganeh and Srinil, 2015). Through a modern reliability methodology (Low and Srinil, 2016), uncertainties in applying wake oscillators to predict flexible cylinder 3-D VIV can also be identified to enhance the confidence in using such a phenomenological model.

Acknowledgement

Insightful and constructive comments from the Editor and anonymous reviewers are gratefully acknowledged.

Appendix A: Finite Difference Scheme

Coupled Eqs. (1)-(3) and (12)-(13), together with Eqs. (4)-(11) may be written in the compact matrix forms as

$$\mathrm{M}\ddot{G} + \mathrm{C}\dot{G} + \mathrm{K_b}G^{IV} + \mathrm{K_{L1}}G' + \mathrm{K_{L2}}G'' = \mathrm{K_N}(G) + \mathrm{F_1}(G, Q) \tag{A1}$$

$$\ddot{Q} - \mathrm{W}\dot{Q} + \mathrm{K_w}Q - \mathrm{F_2}\ddot{G} = -\mathrm{H}(Q) \tag{A2}$$

where $G(Y, t)$ and $Q(Y, t)$ are the vectors of unknown variables (u, v, w) and (p, q), respectively. M is the structural mass, C the structural damping, K_b the bending stiffness, K_{L1} and K_{L2} the axial stiffness, W the wake damping, K_w the shedding frequency and F_2 the structural coupling *linear* matrices whose diagonal components contain (m+m_a), c, EI, -T ′, -T, ($2\varepsilon_u\Omega_f$, $\varepsilon_w\Omega_f$), ($4\Omega_f^2$, Ω_f^2) and (Λ_u/D, Λ_w/D), respectively. In the right-hand terms of Eqs. (A1) and (A2), K_N, F_1 and H are *nonlinear* vectors governing the geometric coupling, the fluid-structure interaction and the van der Pol damping, respectively. Note that K_N is spatially-dependent on the first- and second-order derivatives of displacements whereas F_1 and H are temporally-dependent on the cylinder velocity and wake variables (see Eqs. 14-16).

Using a first-order backward (second-order central) differencing for the temporal (spatial) derivatives (Hoffman and Chiang, 2000), Eqs. (A1) and (A2) can be expanded as

$$\begin{aligned} &\mathrm{M}\frac{G_i^n - 2G_i^{n-1} + G_i^{n-2}}{(\Delta t)^2} + \mathrm{C}\frac{G_i^n - G_i^{n-1}}{\Delta t} \\ &\quad + \mathrm{K_b}\frac{G_{i+2}^n - 4G_{i+1}^n + 6G_i^n - 4G_{i-1}^n + G_{i-2}^n}{(\Delta y)^4} + \mathrm{K_{L1}}\frac{G_{i+1}^n + G_{i-1}^n}{2\Delta y} \\ &\quad + \mathrm{K_{L2}}\frac{G_{i+1}^n - 2G_i^n + G_{i-1}^n}{(\Delta y)^2} \\ &\quad = \mathrm{K_N}(G_{i+1}^n, G_i^n, G_{i-1}^n, \Delta y) + \mathrm{F_1}(G_i^{n-1}, G_i^n, Q_i^n, \Delta t), \end{aligned} \tag{A3}$$

$$\begin{aligned} &\frac{Q_i^n - 2Q_i^{n-1} + Q_i^{n-2}}{(\Delta t)^2} - \mathrm{W}\frac{Q_i^n - Q_i^{n-1}}{\Delta t} + \mathrm{K_w}Q_i^n - \mathrm{F_2}\frac{G_i^n - 2G_i^{n-1} + G_i^{n-2}}{(\Delta t)^2} \\ &\quad = -\mathrm{H}(Q_i^n, Q_i^{n-1}, \Delta t), \end{aligned} \tag{A4}$$

where the subscript i denotes a spatial grid point (node) and the superscript n specifies a step in time. Δy (Δt) is the size of spatial (temporal) discretization. With total N nodes and pinned-pinned boundary conditions (with zero displacements and curvatures) for the flexible cylinder vibrating in 3-D, there are totally 3(N-2) and 2N unknown cylinder and wake variables through Eqs. (A3) and (A4), respectively. By applying initial conditions of displacements and velocities (i.e. with known variables at time n-1 and n-2), Eqs. (A3) and (A4) constitute M (3(N-2)+2N) nonlinear algebraic equations at a particular time step n which read

$$\begin{cases} g_1(G_1^n, G_2^n, G_3^n, \dots, G_i^n, Q_1^n, Q_2^n, Q_3^n, \dots, Q_i^n) = 0 \\ g_2(G_1^n, G_2^n, G_3^n, \dots, G_i^n, Q_1^n, Q_2^n, Q_3^n, \dots, Q_i^n) = 0 \\ \vdots \\ g_M(G_1^n, G_2^n, G_3^n, \dots, G_i^n, Q_1^n, Q_2^n, Q_3^n, \dots, Q_i^n) = 0 \end{cases} \tag{A5}$$

where g_i is the nodal vector function. This system can be iteratively solved using a standard Newton-Raphson method (Yin et al., 2002) which entails

$$\begin{bmatrix} G_{1,k+1}^n \\ G_{2,k+1}^n \\ G_{3,k+1}^n \\ \vdots \\ Q_{i,k+1}^n \end{bmatrix} = \begin{bmatrix} G_{1,k}^n \\ G_{2,k}^n \\ G_{3,k}^n \\ \vdots \\ Q_{i,k}^n \end{bmatrix} - J_k^{-1}\left(g(G_{1,k}^n, G_{2,k}^n, G_{3,k}^n, \dots, G_{i,k}^n, Q_{1,k}^n, Q_{2,k}^n, Q_{3,k}^n, \dots, Q_{i,k}^n)\right) \begin{pmatrix} G_{1,k}^n \\ G_{2,k}^n \\ G_{3,k}^n \\ \vdots \\ Q_{i,k}^n \end{pmatrix} \tag{A6}$$

where the subscript k indicates the iteration step of the Newton-Raphson method and $J^{-1}(..)$ is the inverse of the Jacobian matrix for which

$$J(g) = \begin{bmatrix} \frac{\partial g_1}{\partial G_1^n} & \frac{\partial g_1}{\partial G_2^n} & \cdots & \frac{\partial g_1}{\partial Q_i^n} \\ \frac{\partial g_2}{\partial G_1^n} & \frac{\partial g_2}{\partial G_2^n} & \cdots & \frac{\partial g_2}{\partial Q_i^n} \\ \cdots & \ddots & \ddots & \vdots \\ \frac{\partial g_M}{\partial G_1^n} & \frac{\partial g_M}{\partial G_2^n} & \cdots & \frac{\partial g_M}{\partial Q_i^n} \end{bmatrix} \tag{A7}$$

A non-zero initial guess of the vector is provided and the solution convergence is obtained with a tolerance of 10^{-4}. For the considered flexible cylinder (Song et al., 2011), Δt = 0.0001 s and $\Delta y \approx 0.49$ m have been chosen through a series of convergence studies yielding stable simulations of all considered flow velocities. The solution for each time step through Eq. (A6) is successfully obtained within 15 iterations.

References

Bearman, P.W., 2011. Circular cylinder wakes and vortex-induced vibrations. Journal of Fluids and Structures 27, 648-658.

Bishop, R.E.D., Hassan, A.Y., 1964. The lift and drag forces on a circular cylinder oscillating in a flowing fluid, Proceedings of the Royal Society of London, pp. 51-75.

Blevins, R.D., 1990. Flow-Induced Vibrations. Van Nostrand Reinhold, New York.

Brika, D., Laneville, A., 1993. Vortex-induced vibrations of a long flexible circular cylinder. Journal of Fluid Mechanics 250, 481-508.

Chaplin, J.R., Bearman, P.W., Huera Huarte, F.J., Pattenden, R.J., 2005. Laboratory measurements of vortex-induced vibrations of a vertical tension riser in a stepped current. Journal of Fluids and Structures 21, 3-24.

Currie, I.G., Turnbull, D.H., 1987. Streamwise oscillations of cylinders near the critical Reynolds number. Journal of Fluids and Structures 1, 185-196.

Dahl, J.M., Hover, F.S., Triantafyllou, M.S., Oakley, O.H., 2010. Dual resonance in vortex-induced vibrations at subcritical and supercritical Reynolds numbers, Journal of Fluid Mechanics, pp. 395-424.

Dhanwani, M.A., Sarkar, A., Patnaik, B.S.V., 2013. Lumped parameter models of vortex induced vibration with application to the design of aquatic energy harvester. Journal of Fluids and Structures 43, 302-324.

Facchinetti, M.L., de Langre, E., Biolley, F., 2004. Coupling of structure and wake oscillators in vortex-induced vibrations. Journal of Fluids and Structures 19, 123-140.

Franzini, G.R., Pesce, C.P., Gonçalves, R.T., Fujarra, A.L.C., Pereira, A.A.P., 2014. Concomitant vortex-induced vibration experiments: a cantilevered flexible cylinder and a rigid cylinder mounted on a leaf-spring apparatus. Journal of the Brazilian Society of Mechanical Sciences and Engineering 36, 547-558.

Gabbai, R.D., Benaroya, H., 2005. An overview of modeling and experiments of vortex-induced vibration of circular cylinders. Journal of Sound and Vibration 282, 575-616.

Govardhan, R., Williamson, C., 2006. Defining the 'modified Griffin plot' in vortex-induced vibration: revealing the effect of Reynolds number using controlled damping. Journal of Fluid Mechanics 561, 147-180.

Hoffman, K.A., Chiang, S.T., 2000. Computational Fluid Dynamics Volume I. Engineering Education System.

Huera-Huarte, F.J., 2006. Multi-mode vortex-induced vibrations of a flexible circular cylinder. Imperial College London.

Huera-Huarte, F.J., Bearman, P.W., 2009. Wake structures and vortex-induced vibrations of a long flexible cylinder—Part 1: Dynamic response. Journal of Fluids and Structures 25, 969-990.

Jauvtis, N., Williamson, C.H.K., 2004. The effect of two degrees of freedom on vortex-induced vibration at low mass and damping. Journal of Fluid Mechanics 509, 23-62.

Kim, W.J., Perkins, N.C., 2002. Two-dimensional vortex-induced vibration of cable suspensions. Journal of Fluids and Structures 16, 229-245.

Lie, H., Kaasen, K.E., 2006. Modal analysis of measurements from a large-scale VIV model test of a riser in linearly sheared flow. Journal of Fluids and Structures 22, 557-575.

Low, Y.M., Srinil, N., 2016. VIV fatigue reliability analysis of marine risers with uncertainties in the wake oscillator model. Engineering Structures 106, 96-108.

Mukundan, H., Modarres-Sadeghi, Y., Dahl, J.M., Hover, F.S., Triantafyllou, M.S., 2009. Monitoring VIV fatigue damage on marine risers. Journal of Fluids and Structures 25, 617-628.

Paidoussis, M.P., Price, S.J., de Langre, E., 2011. Fluid-Structure Interactions: Cross-Flow-Induced Instabilities. Cambridge University Press.

Rao, S.S., 2007. Vibration of Continuous Systems. John Wiley & Sons.

Sarpkaya, T., 2004. A critical review of the intrinsic nature of vortex-induced vibrations. Journal of Fluids and Structures 19, 389-447.

Skop, R.A., Balasubramanian, S., 1997. A new twist on an old model for vortex-excited vibrations. Journal of Fluids and Structures 11, 395-412.

Song, J.N., Lu, L., Teng, B., Park, H.I., Tang, G.Q., Wu, H., 2011. Laboratory tests of vortex-induced vibrations of a long flexible riser pipe subjected to uniform flow. Ocean Engineering 38, 1308-1322.

Srinil, N., 2010. Multi-mode interactions in vortex-induced vibrations of flexible curved/straight structures with geometric nonlinearities. Journal of Fluids and Structures 26, 1098-1122.

Srinil, N., 2011. Analysis and prediction of vortex-induced vibrations of variable-tension vertical risers in linearly sheared currents. Applied Ocean Research 33, 41-53.

Srinil, N., Rega, G., 2007. Two-to-one resonant multi-modal dynamics of horizontal/inclined cables. Part II: Internal resonance activation, reduced-order models and nonlinear normal modes. Nonlinear Dynamics 48, 253-274.

Srinil, N., Rega, G., 2008. Nonlinear longitudinal/transversal modal interactions in highly extensible suspended cables. Journal of Sound and Vibration 310, 230-242.

Srinil, N., Rega, G., Chucheepsakul, S., 2004. Three-dimensional non-linear coupling and dynamic tension in the large-amplitude free vibrations of arbitrarily sagged cables. Journal of Sound and Vibration 269, 823-852.

Srinil, N., Rega, G., Chucheepsakul, S., 2007. Two-to-one resonant multi-modal dynamics of horizontal/inclined cables. Part I: Theoretical formulation and model validation. Nonlinear Dynamics 48, 231-252.

Srinil, N., Wiercigroch, M., O'Brien, P., 2009. Reduced-order modelling of vortex-induced vibration of catenary riser. Ocean Engineering 36, 1404-1414.

Srinil, N., Zanganeh, H., 2012. Modelling of coupled cross-flow/in-line vortex-induced vibrations using double Duffing and van der Pol oscillators. Ocean Engineering 53, 83-97.

Srinil, N., Zanganeh, H., Day, A., 2013. Two-degree-of-freedom VIV of circular cylinder with variable natural frequency ratio: Experimental and numerical investigations. Ocean Engineering 73, 179-194.

Swithenbank, S.B., Vandiver, J.K., Larsen, C.M., Lie, H., 2008. Reynolds number dependence of flexible cylinder VIV response data, The 27th International Conference on Offshore Mechanics and Arctic Engineering, pp. OMAE2008-57045.

Tognarelli, M.A., Slocum, S.T., Frank, W.R., Campbell, R.B., 2004. VIV Response of a Long Flexible Cylinder in Uniform and Linearly Sheared Currents. Offshore Technology Conference.

Vandiver, J.K., 1993. Dimensionless parameters important to the prediction of vortex-induced vibration of long, flexible cylinders in ocean currents. Journal of Fluids and Structures 7, 423-455.

Vandiver, J.K., Jaiswal, V., Jhingran, V., 2009. Insights on vortex-induced, traveling waves on long risers. Journal of Fluids and Structures 25, 641-653.

Violette, R., de Langre, E., Szydlowski, J., 2007. Computation of vortex-induced vibrations of long structures using a wake oscillator model: Comparison with DNS and experiments. Computers & Structures 85, 1134-1141.

Williamson, C.H.K., Govardhan, R., 2004. Vortex-induced vibrations. Annual Review of Fluid Mechanics 36, 413-455.

Wu, X., Ge, F., Hong, Y., 2012. A review of recent studies on vortex-induced vibrations of long slender cylinders. Journal of Fluids and Structures 28, 292-308.

Xu, W.-H., Zeng, X.-H., Wu, Y.-X., 2008. High aspect ratio (L/D) riser VIV prediction using wake oscillator model. Ocean Engineering 35, 1769-1774.

Yin, J.-H., Zhu, J.-G., Graham, J., 2002. A new elastic viscoplastic model for time-dependent behaviour of normally and overconsolidated clays: theory and verification. Canadian Geotechnical Journal 39, 157-173.

Zanganeh, H., Srinil, N., 2014. Characterization of variable hydrodynamic coefficients and maximum responses in two-dimensional vortex-induced vibrations with dual resonances. Journal of Vibration and Acoustics 136, 051010.

Zanganeh, H., Srinil, N., 2015. Coupled axial/lateral VIV of marine risers in sheared currents, The 34th International Conference on Ocean, Offshore & Arctic Engineering, St John's, pp. OMAE2015-41606.

Captions of Tables and Figures

Table 1: Summary of transverse bending and longitudinal stresses inclusive of mean and oscillatory components.

Table 2: Summary of transverse bending and longitudinal stresses accounting for only oscillatory components.

Fig.1: (a) A schematic 3-D model of a flexible cylinder undergoing VIV and sectional hydrodynamic forces for (b) stationary cylinder and (c, d) oscillating cylinder with (c) 3-D or (d) 2-D force projection.

Fig.2: Comparison of space-time varying responses with 2-D (a-e) vs 3-D (f-j) force projection models at V = 1 m/s: (a, f) CF response, (b, g) IL response, (c, h) AX response, (d, i) IL response with removed mean values, (e, j) AX response with removed mean values.

Fig.3: Space-time varying responses accounting for initial transients, mean and oscillatory components for (a, d) CF, (b, e) IL and (c, f) AX VIV at low and high V.

Fig.4: Space-time varying responses with extracted steady-state oscillatory components for (a-d) CF, (e-h) IL and (i-l) AX VIV at various V.

Fig.5: Oscillation frequencies associated with responses in Fig. 4 for (a-d) CF, (e-h) IL and (i-l) AX VIV at various V.

Fig.6: Multi modal decomposition of VIV responses in Figs. 4 and 5: circulars, squares and stars denote CF, IL and AX modes, respectively.

Fig.7: Spatial variation of IL-CF, IL-AX and CF-AX trajectories associated with responses in Fig. 4 at low and high V.

Fig.8: Spatial (a) IL mean and (b) AX mean displacements with varying V.

Fig.9: Space-time varying (a, d) CF bending, (b, e) IL bending and (c, f) longitudinal stresses (in MPa) inclusive of mean and oscillatory components.

Fig.10: Effect of geometric nonlinearities and axial dynamics on flexible cylinder VIV with circulars, squares and diamonds denoting the full nonlinear model with axial motions, the geometrically-linearized model with axial motions and the full nonlinear model without axial motions, respectively: (a, c) CF and (b, d) IL RMS responses; (e) in-line mean displacements.

Fig.11: Individual effect of axial motions, geometric and hydrodynamic nonlinearities on CF (a-c) and IL (d-f) VIV by considering (a, d) the full nonlinear model without axial motion, (b, e) the linear hydrodynamic model without axial motion and (c, f) the linear geometric-hydrodynamic model without axial motion.

Fig.12: Comparison of numerical prediction and experimental results with (a, b) maximum and (c, d) RMS amplitudes of (a, c) CF and (b, d) IL VIV.

Fig.13: Comparison of numerical prediction and experimental results with dominant (a) oscillation frequencies and (b) excited VIV modes.

Table 1

V (m/s)	CF bending stress (MPa)		IL bending stress (MPa)		Longitudinal stress (MPa)	
	Max	Min	Max	Min	Max	Min
0.3	8.3	-8.3	2.5	-7.7	26.9	21.8
0.4	13.6	-13.6	5.5	-12.7	47.4	39.7
0.8	26.1	-26.1	8.2	-29.1	142.1	130.2
1.0	30.4	-30.4	8.8	-34.6	205.2	184.2

Table 2

V (m/s)	CF bending stress (MPa)		IL bending stress (MPa)		Longitudinal stress (MPa)	
	Max	Min	Max	Min	Max	Min
0.3	8.3	-8.3	4.1	-3.0	2.4	-2.7
0.4	13.6	-13.6	7.6	-6.6	3.6	-4.1
0.8	26.1	-26.1	13.9	-15.1	5.1	-5.5
1.0	30.4	-30.4	17.6	-16.5	9.3	-7.7

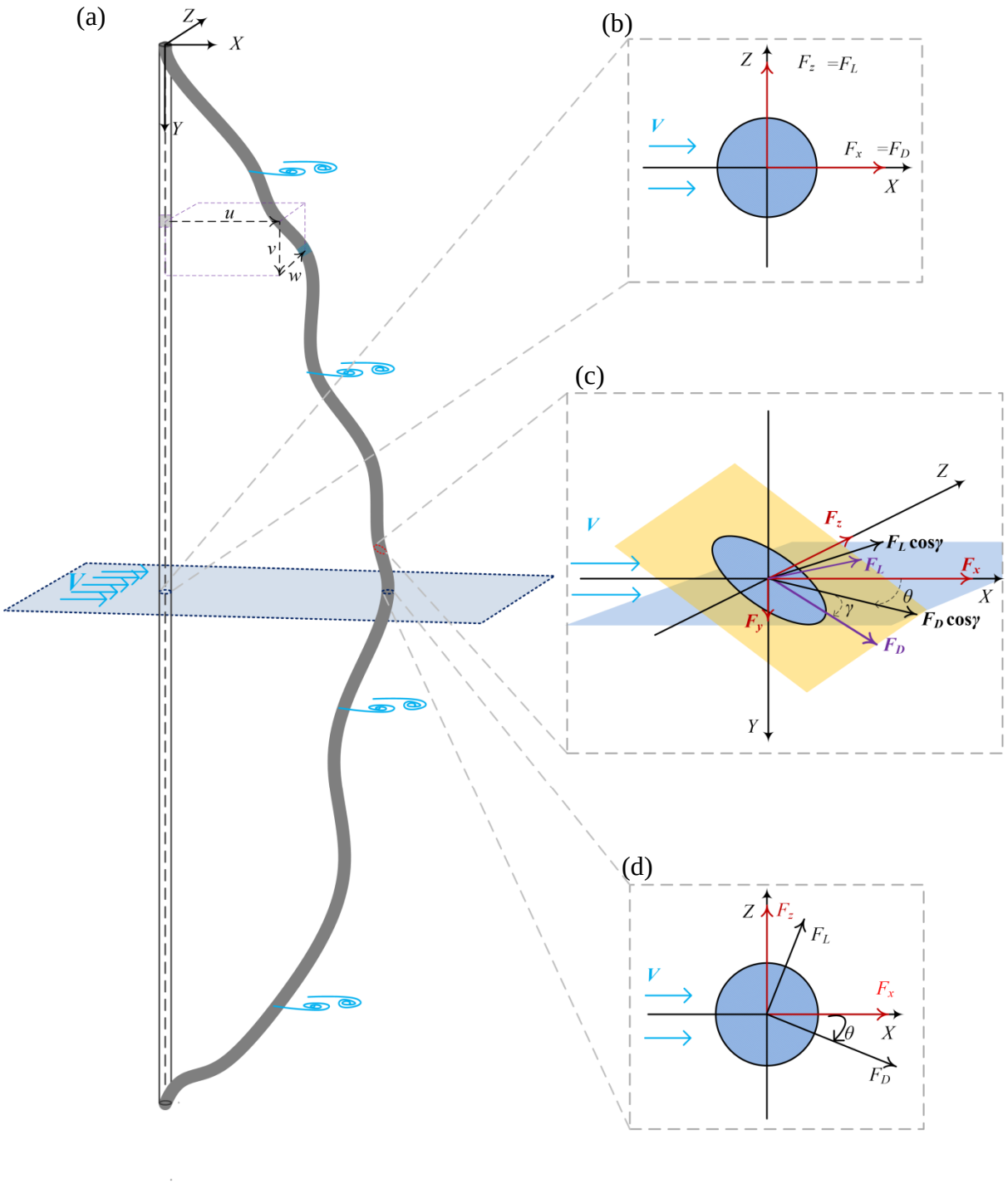
(a)
Z
X
Y
u
v
w
V
(b)
Z
$F_z = F_L$
V
$F_x = F_D$
X
(c)
Z
V
F_z
$F_L \cos\gamma$
F_L
F_x
X
θ
γ
F_y
$F_D \cos\gamma$
F_D
Y
(d)
Z
F_z
F_L
V
F_x
θ
X
F_D

Figure 1

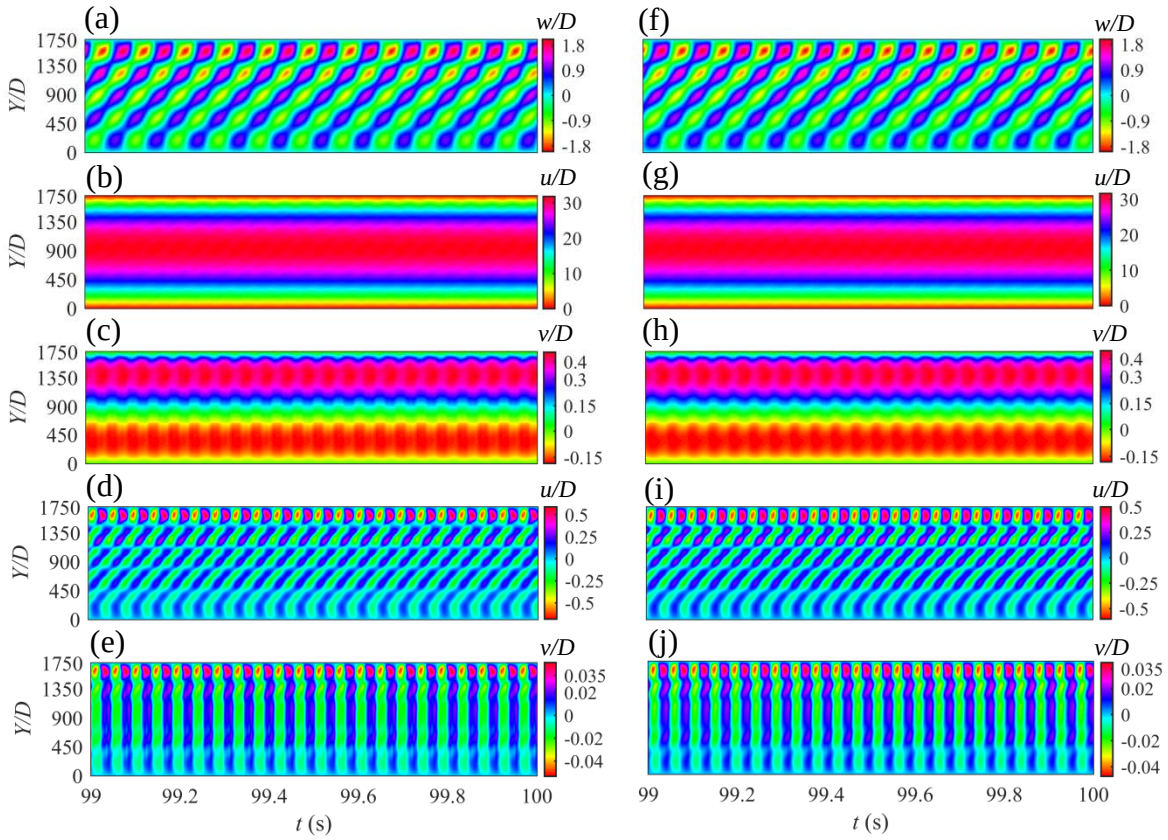
(a)
w/D
1.8
0.9
0
-0.9
-1.8
(b)
u/D
30
20
10
0
(c)
v/D
0.4
0.3
0.15
0
-0.15
(d)
u/D
0.5
0.25
0
-0.25
-0.5
(e)
v/D
0.035
0.02
0
-0.02
-0.04
(f)
w/D
(g)
u/D
(h)
v/D
(i)
u/D
(j)
v/D
Y/D
1750
1350
900
450
0
99
99.2
99.4
99.6
99.8
100
t (s)

Figure 2

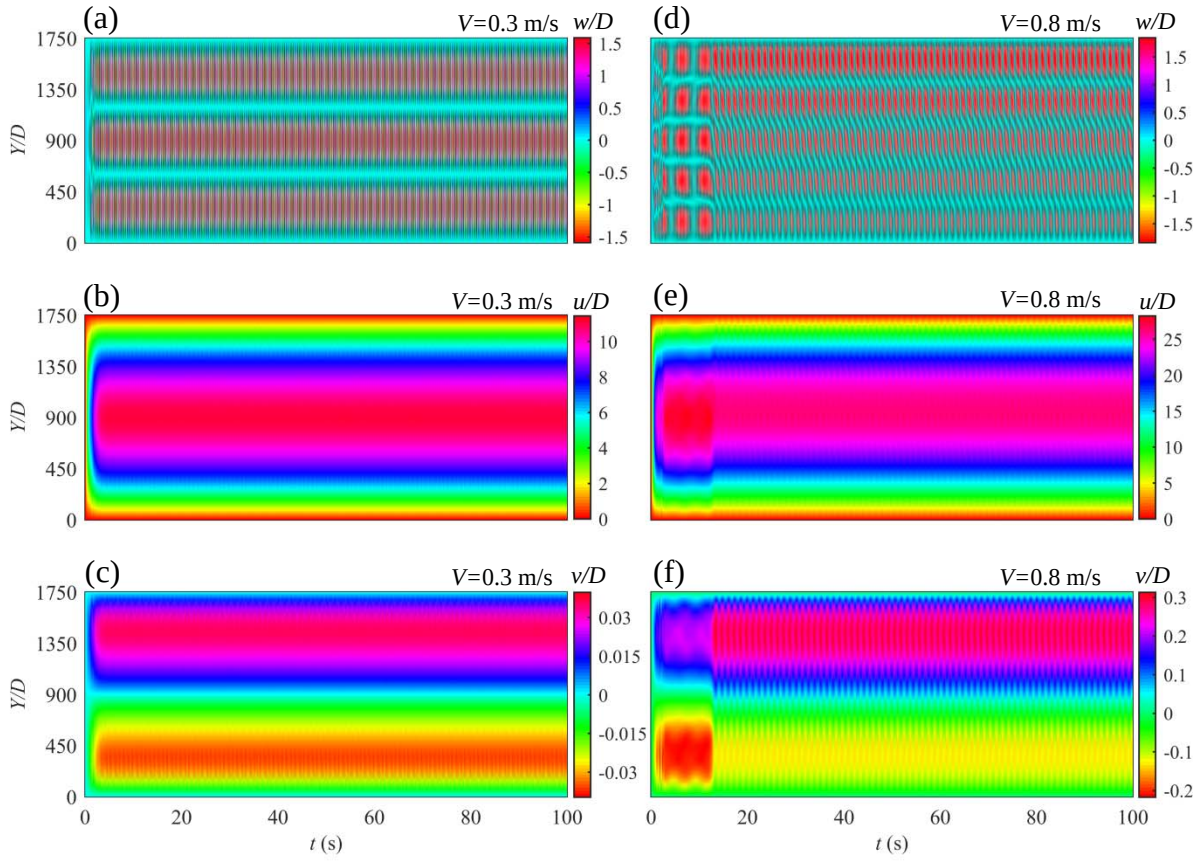
(a)
V=0.3 m/s
w/D
(d)
V=0.8 m/s
w/D
(b)
V=0.3 m/s
u/D
(e)
V=0.8 m/s
u/D
(c)
V=0.3 m/s
v/D
(f)
V=0.8 m/s
v/D
Y/D
t (s)

Figure 3

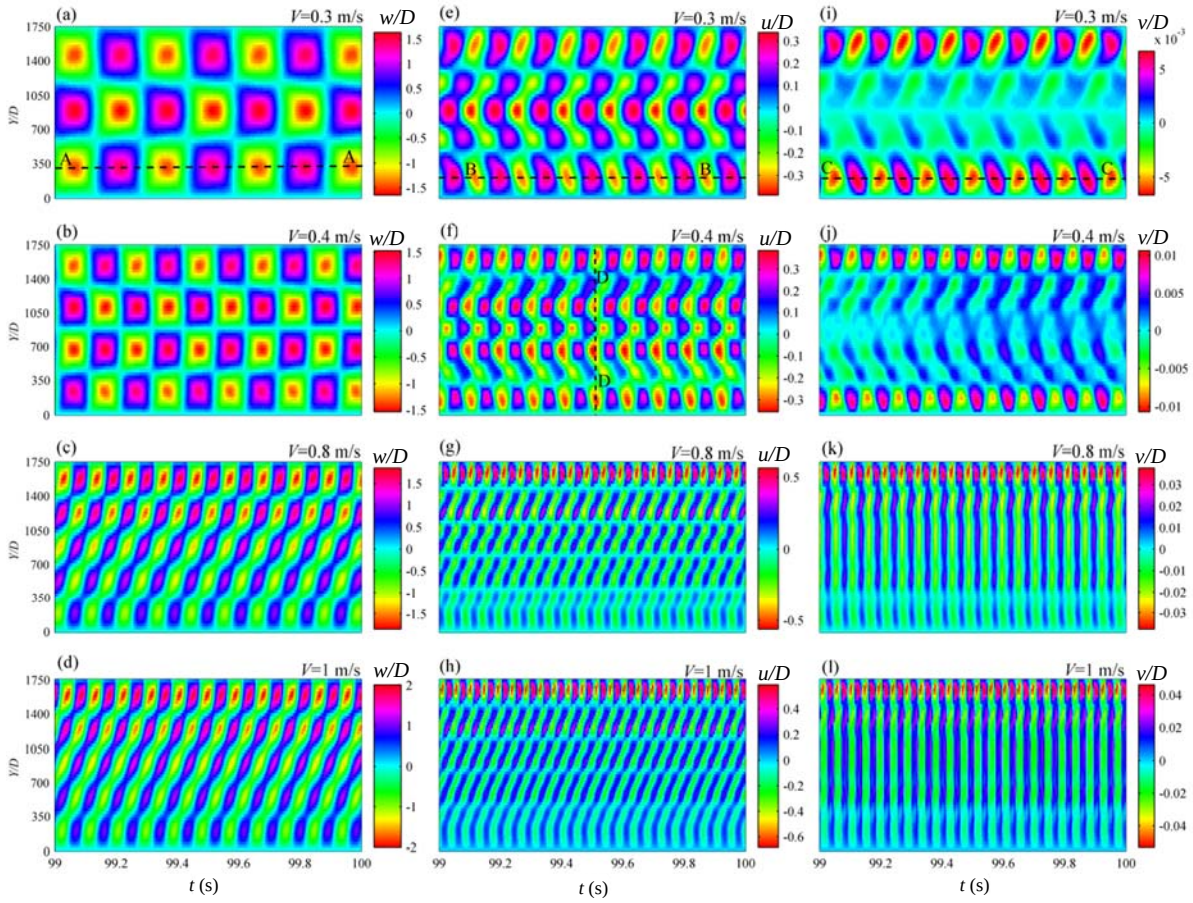
(a)
V=0.3 m/s
w/D
(e)
V=0.3 m/s
u/D
(i)
V=0.3 m/s
v/D
(b)
V=0.4 m/s
w/D
(f)
V=0.4 m/s
u/D
(j)
V=0.4 m/s
v/D
(c)
V=0.8 m/s
w/D
(g)
V=0.8 m/s
u/D
(k)
V=0.8 m/s
v/D
(d)
V=1 m/s
w/D
(h)
V=1 m/s
u/D
(l)
V=1 m/s
v/D
Y/D
t (s)
A
B
C
D

Figure 4

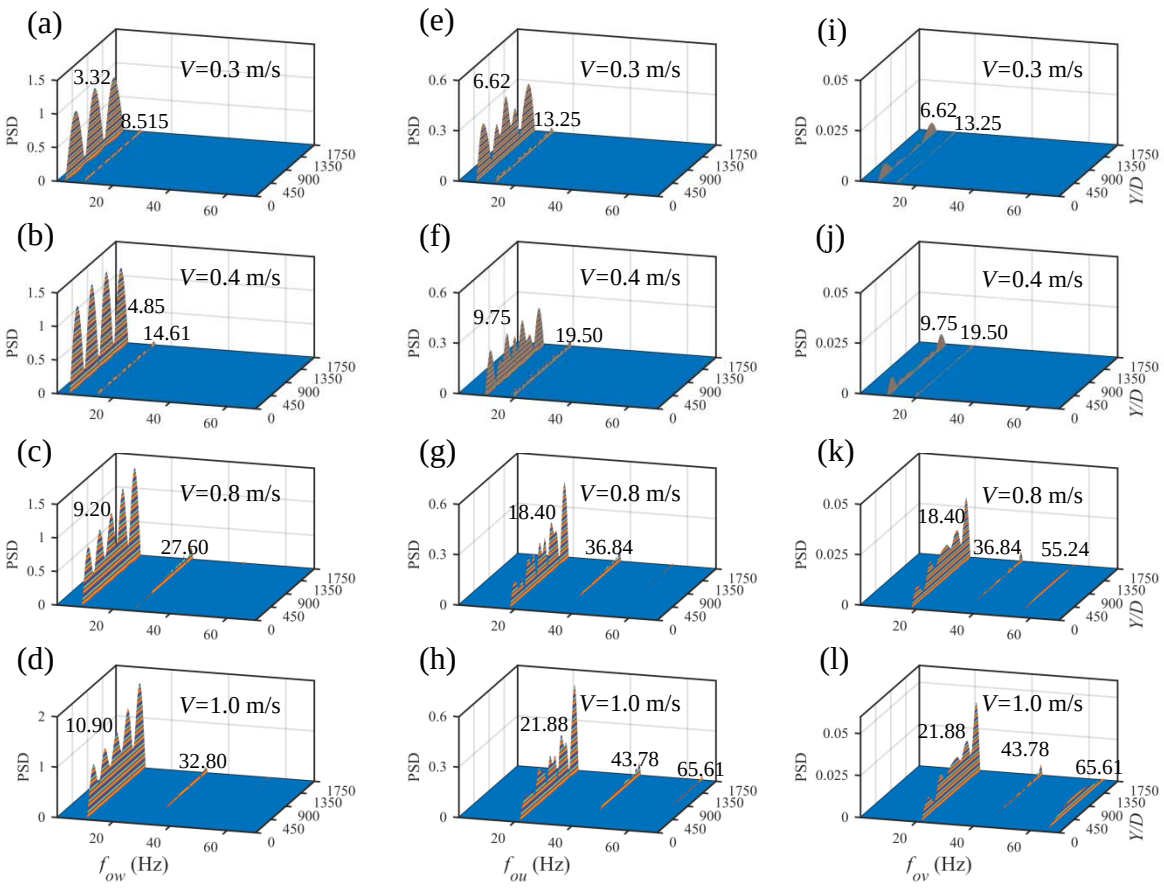
(a)
V=0.3 m/s
3.32
8.515
(b)
V=0.4 m/s
4.85
14.61
(c)
V=0.8 m/s
9.20
27.60
(d)
V=1.0 m/s
10.90
32.80
(e)
V=0.3 m/s
6.62
13.25
(f)
V=0.4 m/s
9.75
19.50
(g)
V=0.8 m/s
18.40
36.84
(h)
V=1.0 m/s
21.88
43.78
65.61
(i)
V=0.3 m/s
6.62
13.25
(j)
V=0.4 m/s
9.75
19.50
(k)
V=0.8 m/s
18.40
36.84
55.24
(l)
V=1.0 m/s
21.88
43.78
65.61
PSD
Y/D
f_ow (Hz)
f_ou (Hz)
f_ov (Hz)

Figure 5

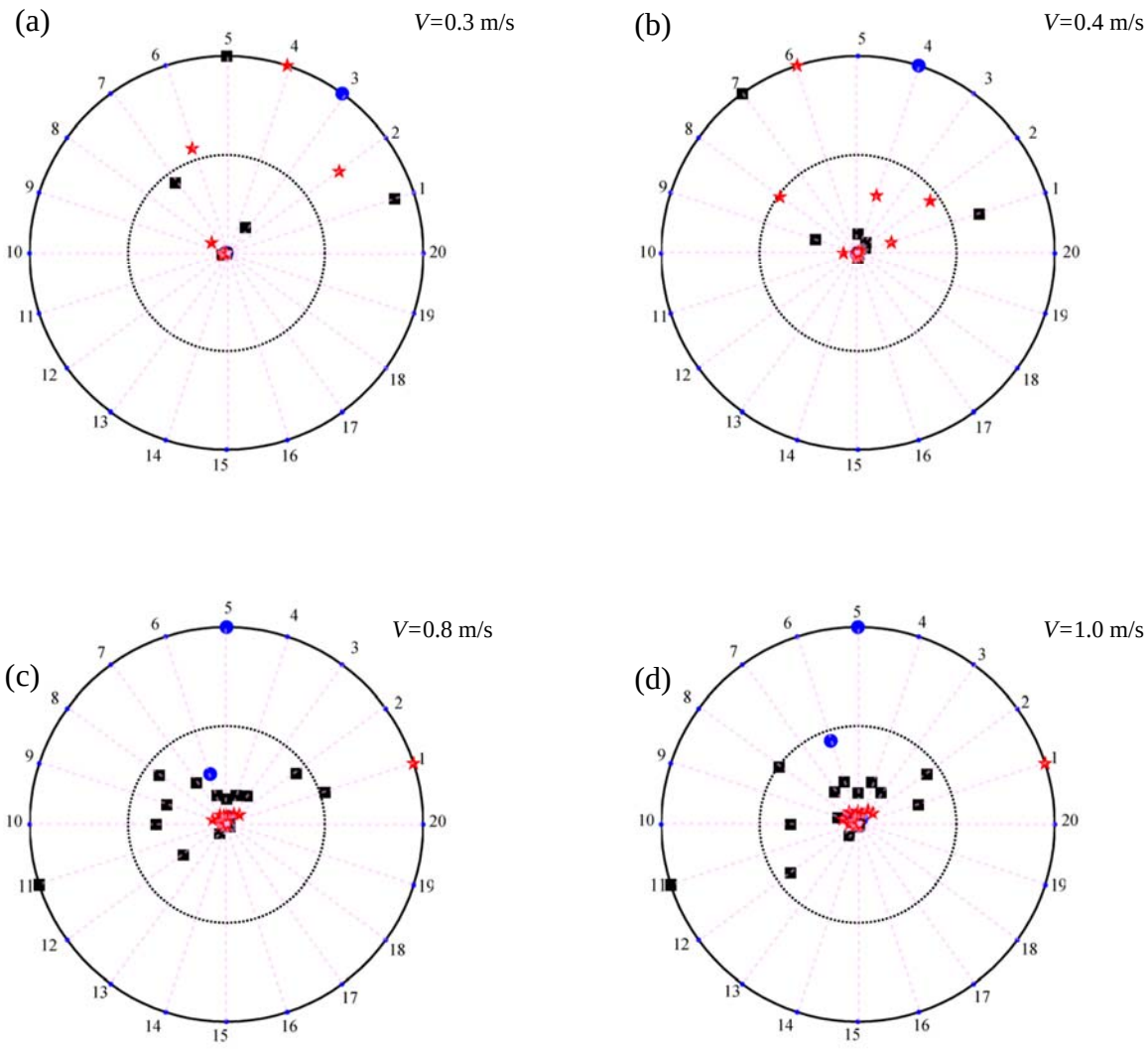

Figure 6

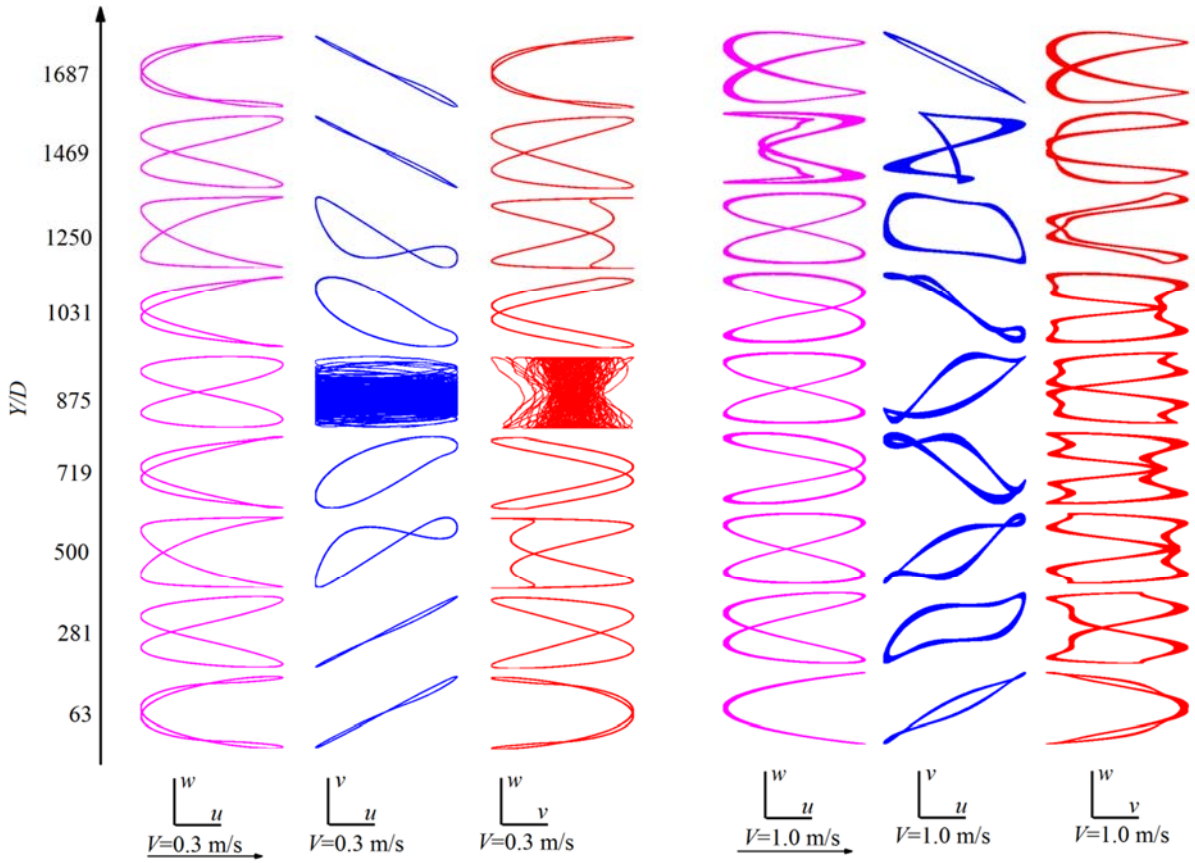
Y/D
1687
1469
1250
1031
875
719
500
281
63
w
u
V=0.3 m/s
v
u
V=0.3 m/s
w
v
V=0.3 m/s
w
u
V=1.0 m/s
v
u
V=1.0 m/s
w
v
V=1.0 m/s

Figure 7

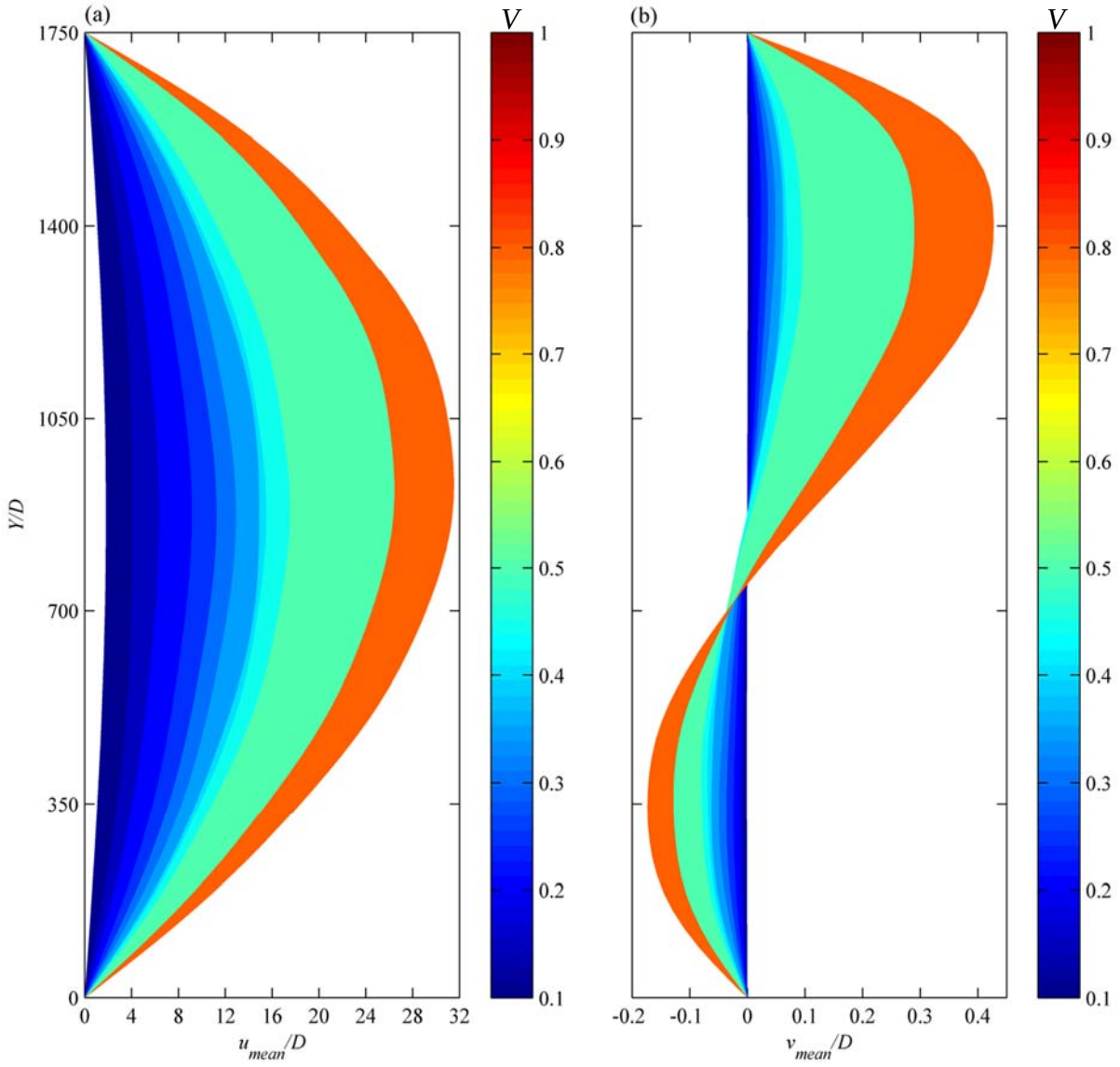
(a)
(b)
V
Y/D
1750
1400
1050
700
350
0
0
4
8
12
16
20
24
28
32
u_{mean}/D
-0.2
-0.1
0
0.1
0.2
0.3
0.4
v_{mean}/D
1
0.9
0.8
0.7
0.6
0.5
0.4
0.3
0.2
0.1

Figure 8

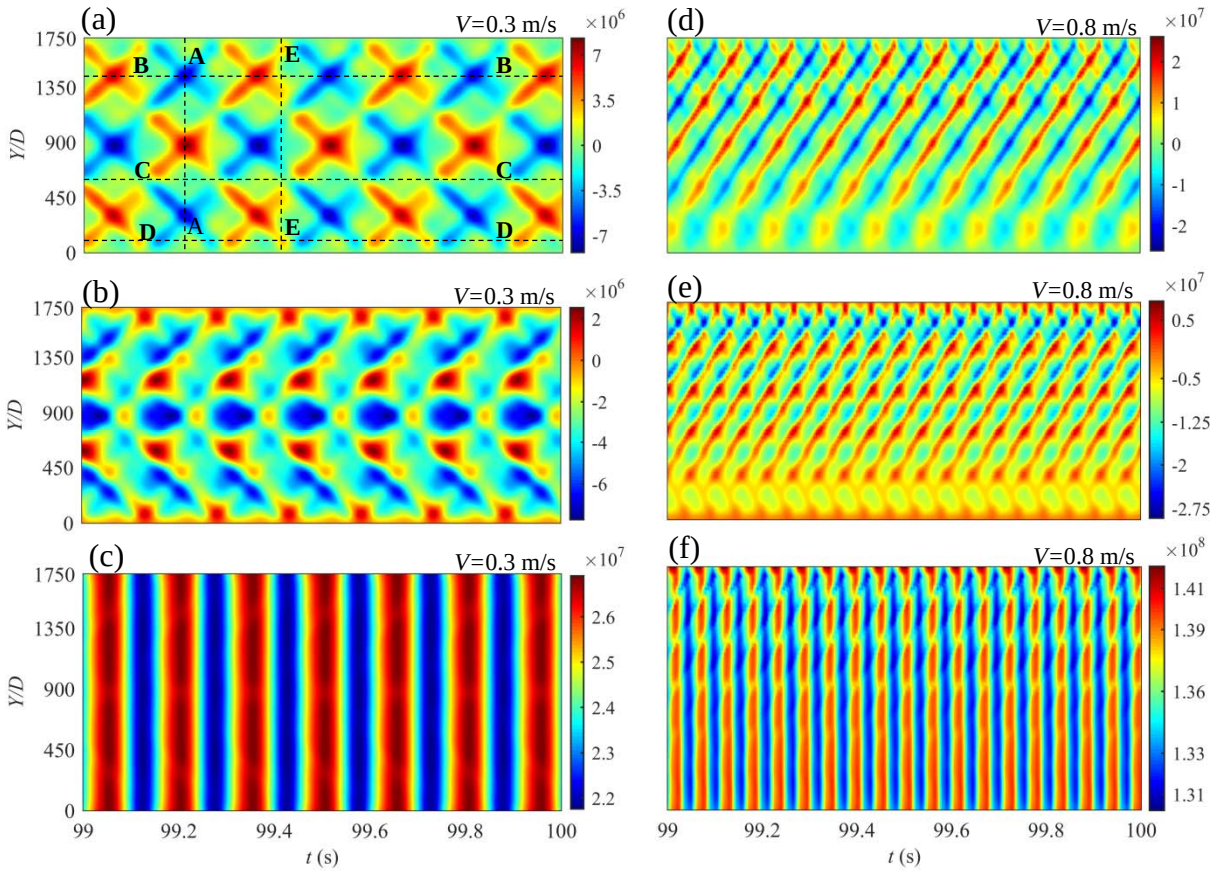
(a)
V=0.3 m/s
×10^6
7
3.5
0
-3.5
-7
B
A
E
B
C
C
D
A
E
D
(b)
V=0.3 m/s
×10^6
2
0
-2
-4
-6
(c)
V=0.3 m/s
×10^7
2.6
2.5
2.4
2.3
2.2
(d)
V=0.8 m/s
×10^7
2
1
0
-1
-2
(e)
V=0.8 m/s
×10^7
0.5
-0.5
-1.25
-2
-2.75
(f)
V=0.8 m/s
×10^8
1.41
1.39
1.36
1.33
1.31
Y/D
1750
1350
900
450
0
99
99.2
99.4
99.6
99.8
100
t (s)

Figure 9

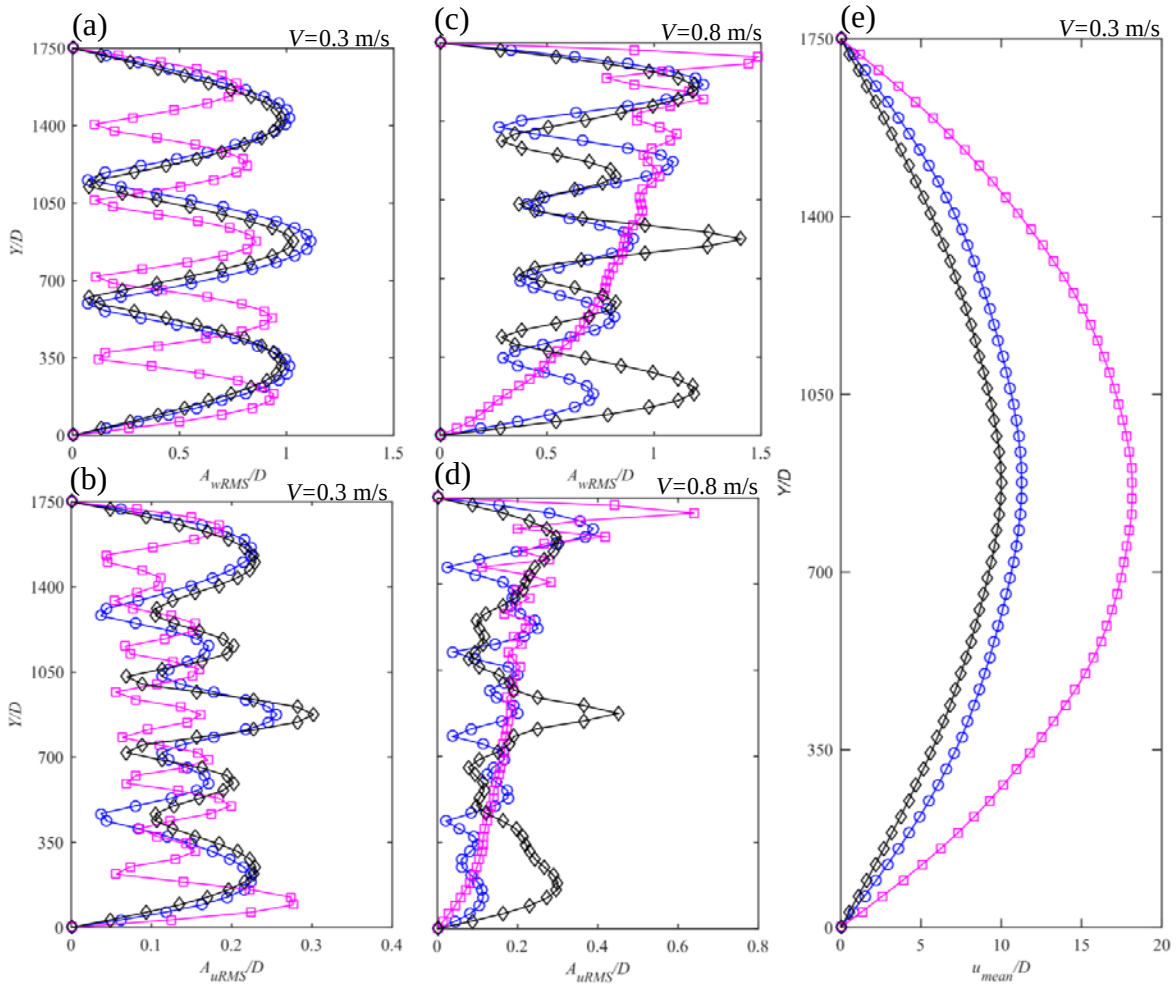
(a)
V=0.3 m/s
(c)
V=0.8 m/s
(e)
V=0.3 m/s
(b)
V=0.3 m/s
(d)
V=0.8 m/s
Y/D
A_wRMS/D
A_uRMS/D
u_mean/D

Figure 10

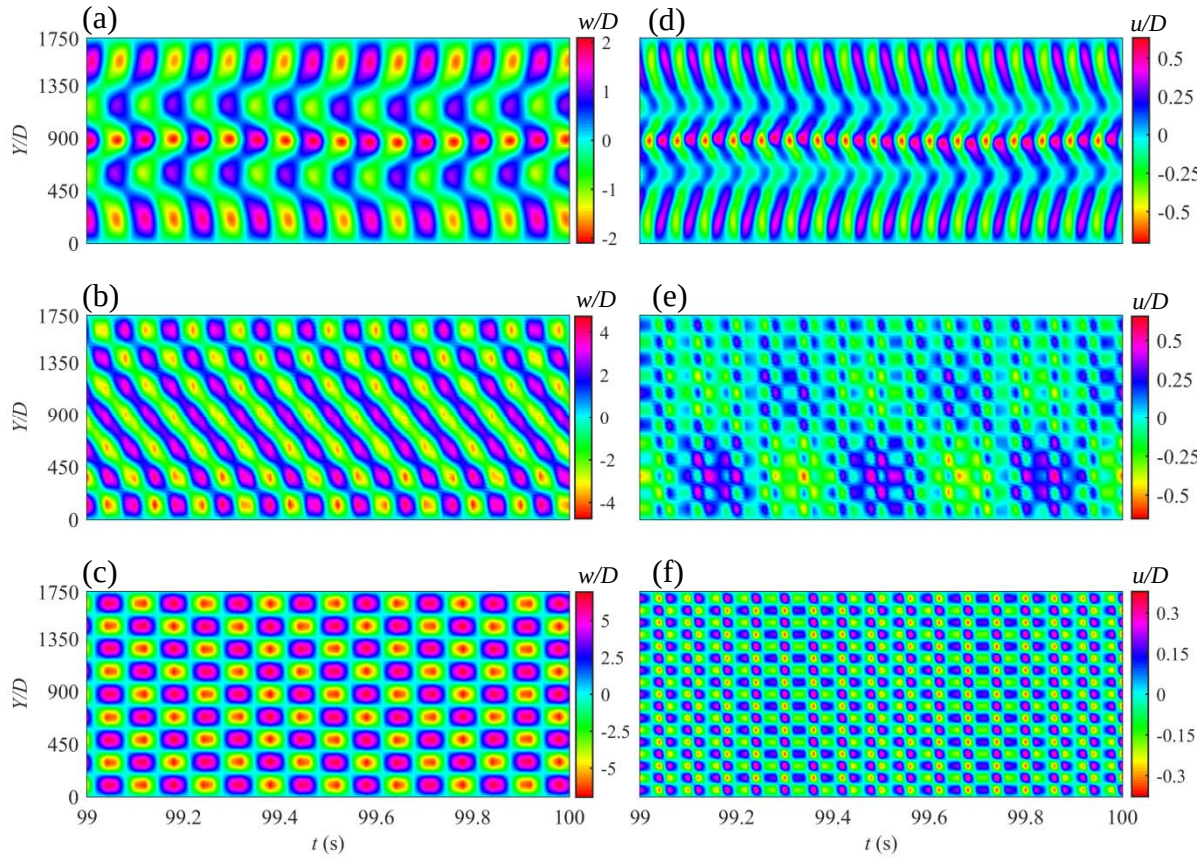
(a)
(b)
(c)
(d)
(e)
(f)
w/D
u/D
Y/D
t (s)
1750
1350
900
450
0
99
99.2
99.4
99.6
99.8
100
2
1
0
-1
-2
4
-4
5
2.5
-2.5
-5
0.5
0.25
-0.25
-0.5
0.3
0.15
-0.15
-0.3

Figure 11

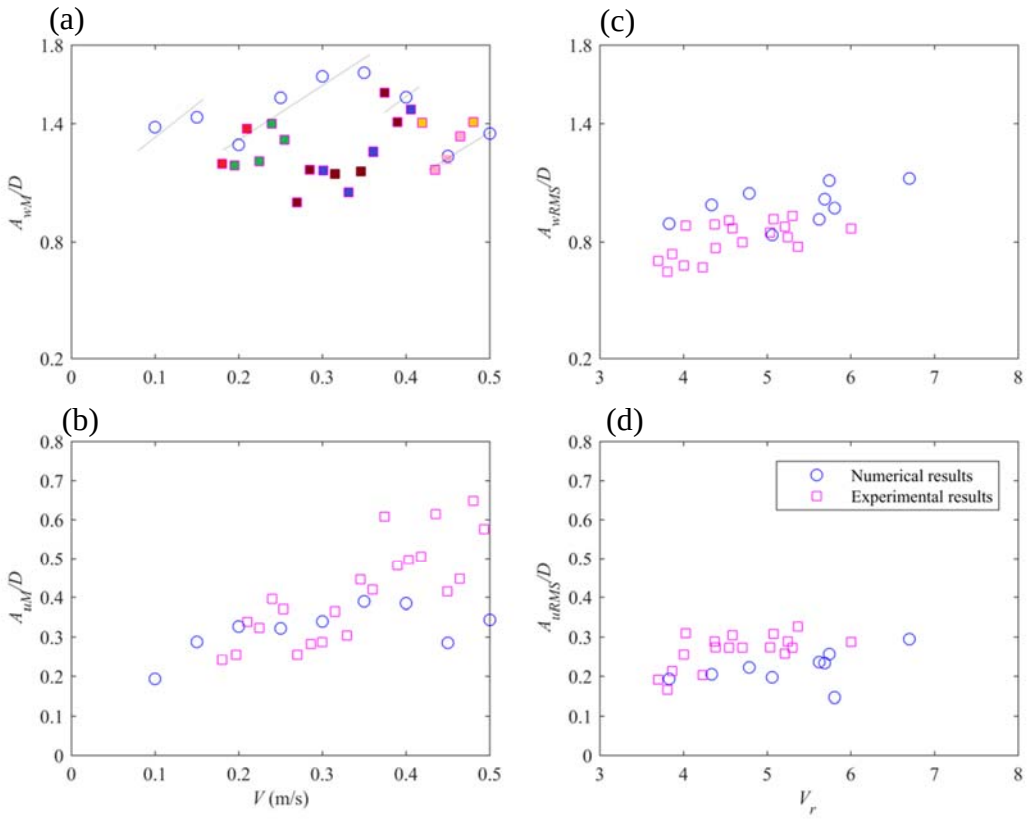
(a)
(c)
(b)
(d)
A_{wM}/D
A_{wRMS}/D
A_{uM}/D
A_{uRMS}/D
V (m/s)
V_r
Numerical results
Experimental results

Figure 12

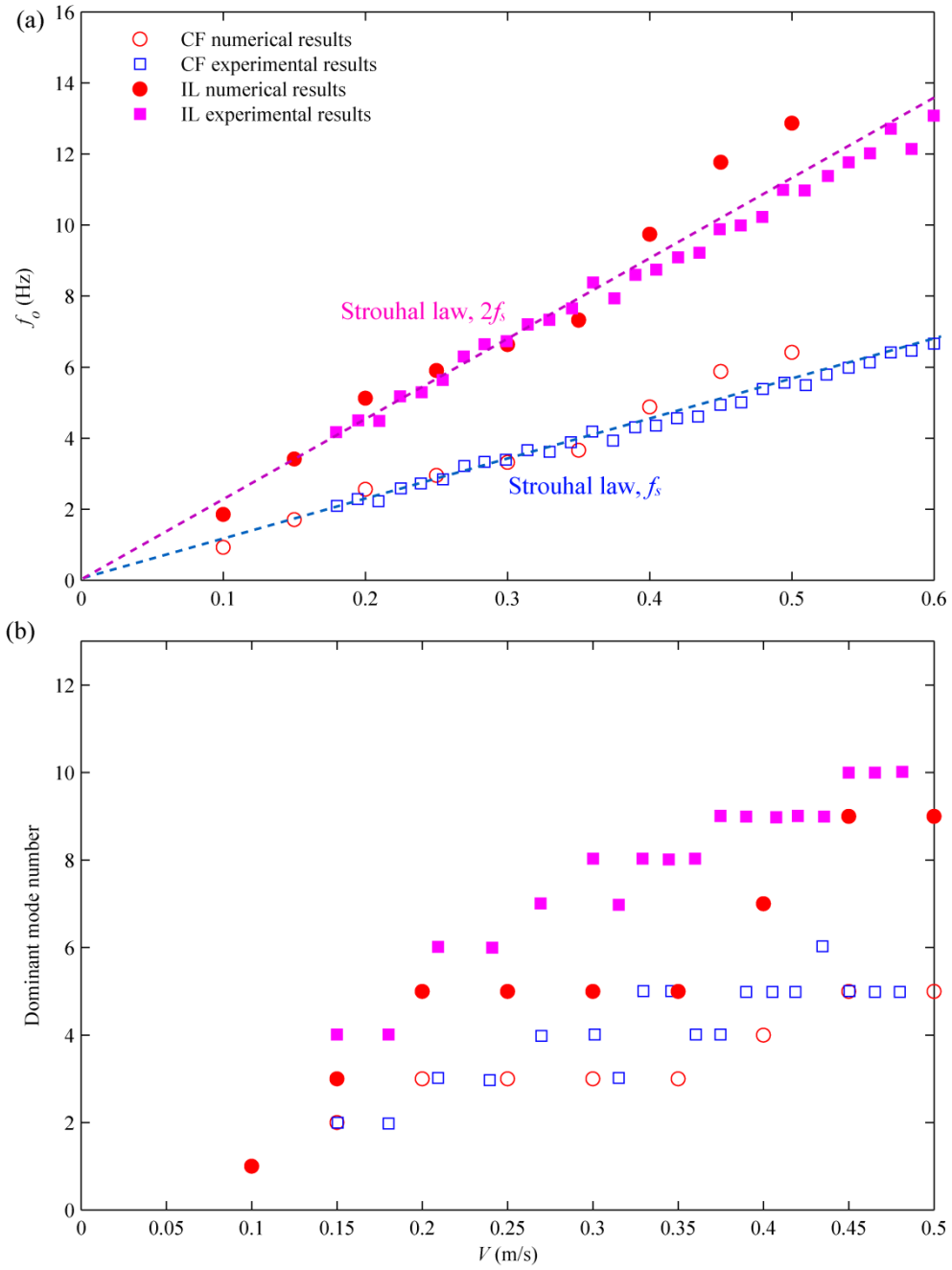
(a)
CF numerical results
CF experimental results
IL numerical results
IL experimental results
Strouhal law, 2fs
Strouhal law, fs
fo (Hz)
(b)
Dominant mode number
V (m/s)

Figure 13